Journal of *Marine Science and Engineering*

MDPI

Article

Sedimentary Environment, Tectonic Setting, and Uranium Mineralization Implications of the Yimin Formation, Kelulun Depression, Hailar Basin, China

Fanmin Meng [1], Fengjun Nie [1,2,*], Fei Xia [1,2], Zhaobin Yan [1,2], Da Sun [1,2], Wenbo Zhou [3], Xin Zhang [1,2] and Qing Wang [1]

[1] School of Earth Sciences, East China University of Technology, Nanchang 330013, China; 18702625683@163.com (F.M.); fxia@ecut.edu.cn (F.X.); zbyan@ecut.edu.cn (Z.Y.); sunda0214@163.com (D.S.); zhangxin@ecut.edu.cn (X.Z.); destinw@126.com (Q.W.)
[2] State Key Laboratory of Nuclear Resources and Environment, East China University of Technology, Nanchang 330013, China
[3] Geological Party No. 243, China National Nuclear Corporation, Chifeng 024000, China; 313363600@163.com
* Correspondence: niefj@263.net

Abstract: The sandstone-type uranium deposit of the Kelulun Depression is the first industrially valuable uranium deposit discovered in the Hailar Basin. This study performed a systematic examination of 17 sandstone samples from the Yimin Formation in the Kelulun Depression based on various analytical techniques. The findings of the current study were synthesized with previous research to investigate the impact of the redox conditions and the tectonic background of the source area, as well as the paleoclimatic evolution of the Yimin Formation on uranium mineralization. The elemental Mo, U/Th, V/Cr, Ni/Co, and V/(V + Ni) ratios indicate that the paleowater was in an oxygen-rich environment during the deposition of the Yimin Formation. Additionally, the C-value, Sr/Cu, Al_2O_3/MgO, and Rb/Sr ratios indicate that the Yimin Formation was formed in a paleoclimate characterized by arid-to-semi-arid conditions. The geochemical characteristics of the observed elements indicated that the sediment source of the Yimin Formation was mainly felsic rocks from the upper continental crust, the weathering of the rock was weak, and the tectonic background was a passive continental margin. Coffinite is distributed in the form of cementation and stellates within or around pyrite crystals, and uranium-titanium oxide is mostly distributed in an irregular granular distribution in the biotite cleavage fractures of the study area. In summary, the findings of this study reveal that the tectonic settings, provenance, uranium source, paleoclimate, and oxygen-rich paleowater of the Yimin Formation have important geological significance for the large-scale uranium mineralization of the Kelulun Depression.

Keywords: Yimin formation; geochemistry; sandstone-type uranium deposit; provenance analysis; paleoclimate; Kelulun depression

Citation: Meng, F.; Nie, F.; Xia, F.; Yan, Z.; Sun, D.; Zhou, W.; Zhang, X.; Wang, Q. Sedimentary Environment, Tectonic Setting, and Uranium Mineralization Implications of the Yimin Formation, Kelulun Depression, Hailar Basin, China. *J. Mar. Sci. Eng.* **2024**, *12*, 763. https://doi.org/10.3390/jmse12050763

Academic Editor: Anabela Oliveira

Received: 25 March 2024
Revised: 27 April 2024
Accepted: 29 April 2024
Published: 30 April 2024

1. Introduction

The Hailar Basin is a terrestrial rift basin that is rich in coal, oil, and natural gas. In recent years, significant advancements have been made in mineral exploration, leading to the discovery of large-scale sandstone-type uranium mineralizations within the Cretaceous layers of the Hailar Basin. Many uranium ore sites and mineralization points have recently been discovered in the Kelulun Depression, which is located in the southwestern part of the basin. The distribution of the uranium mineralizations is such that they mostly occur within the Cretaceous strata of the Yimin Formation. Numerous prior investigations have been conducted on the sandstone-type uranium in the region, with a primary emphasis on identifying the target layer [1], characterizing the sand body [2], assessing the hydrogeological conditions [3], conducting airborne radioactivity measurements [4], and analyzing

the potential for uranium mineralization [5–7]. Nonetheless, the lack of comprehensive investigations on the geochemical characteristics, provenance, paleoclimate, varieties, and forms of uranium minerals in the ore-bearing target layers has hindered the precise determination of the correlation between the sandstones found in the Yimin Formation and the mineralization of uranium. Consequently, this limitation has impeded our understanding of the association between the sandstones of the Yimin Formation within the basin and the extensive uranium mineralization that occurred within the basin.

The exploration of sandstone-type uranium deposits has revealed that the sedimentation of surface water systems plays a crucial role in connecting uranium sources with sedimentary basins [8]. This process effectively limits the transportation of uranium, as demonstrated in previous studies [9–12]. A thorough investigation of the redox conditions of ancient water bodies is important for elucidating the process of the mineralization of sandstone [13–15]. Furthermore, certain elements present in clastic sedimentary rocks did not undergo substantial migration throughout the process of long-distance transportation. Consequently, these elements are valuable sources of information [16–18]. The presence of trace elements and their concentrations in sediments can serve as valuable indicators of past environmental and climatic variations. These indicators can effectively inform us about the source materials and provenance structural characteristics of, as well as the interplay between, orogenic processes and basin development in sedimentary basins. Therefore, this paper focuses on the Yimin Formation, located in the Kelulun Depression of the Hailar Basin, as its subject of investigation. Representative samples of the Yimin Formation were collected and various methodologies, including petrology, geochemistry, and electron probe microanalysis, were employed to conduct a comprehensive study. Furthermore, by analyzing the vertical variations in trace and rare earth elements, this study attempts to reconstruct the processes of formation of paleowater bodies and paleoclimate fluctuations. Additionally, this study aims to investigate the interplay between regional tectonic activity and paleo-sedimentary environments. The findings presented in this study are important for elucidating the involvement of paleo-sedimentary and paleoclimatic conditions in the process of uranium mineralization inside the Kelulun Depression.

2. Geological Background

Hailar Basin, which is located in the eastern section of the Central Asian orogenic belt (Figure 1a), is a Cenozoic continental rift basin that developed on the Paleozoic collisional orogenic belt between the Siberian and North China plates [1]. The basin has experienced four distinct development stages since its initial formation, which can be attributed to the influence of the north-east-trending Delbugan and Erguna fault zones. These stages included Late Jurassic rifting, Early Cretaceous depression, late Early Cretaceous shrinkage, and Late Cretaceous-Neogene differential uplift and leveling [19,20]. Finally, the basin has acquired a tectonic framework characterized by a "two uplifts and three depressions" configuration [1].

The Kelulun Depression, situated within the Zhabenuoer depression in the Southwestern Hailar Basin, is a separate second-order negative secondary structural unit. This depression is characterized by its elongated shape resembling a dustpan, with a narrow width and northeast-oriented distribution (Figure 1b) [21]. The depression is connected to the Adunchulu uplift in the west, the Han Wula bulge in the east, and the Hulun Lake depression in the north, and extends to the basin boundary in the south (Figure 1c). Tectonic activity in the early and middle stages of the depression's sedimentation in the Early Cretaceous was strong and generated more than 40 different types of fractures. The fracture system can be divided into three groups according to the direction of the fracture plane spread: north-northeast, north-east, and north-south. The north-east trending fault system is consistent with the main distribution direction of the Kelulun Depression and controls the current structural pattern of the depression [22]. Moreover, it is the main controlling fault system in the area and is characterized by an early formation and long development times. The fracture system of this group cuts through the Jurassic to the Quaternary, thus

providing a channel for the transportation of ore-bearing fluids and the uplift of reducing materials, such as oil and gas, in the deeper parts of the area. The basin's basement is dominated by Paleozoic metamorphic rocks and Hercynian granites. Large numbers of Hercynian granites and intermediate acidic volcanic rocks are distributed around the basin rim, and they have a high uranium content [23]. The sedimentary cover consists of the Cretaceous Nantun Formation (K_1n), the Tongbomiao Formation (K_1t), the Damoguaihe Formation (K_1d), the Yimin Formation (K_1y), the Neogene Huchashan Formation (N_2h), and Quaternary formations (Q) from bottom to top. The Cretaceous Yimin Formation is a set of dark coal-bearing clastic sedimentary rocks with a high reduction capacity and represents the main uranium-bearing layer in the basin [24,25].

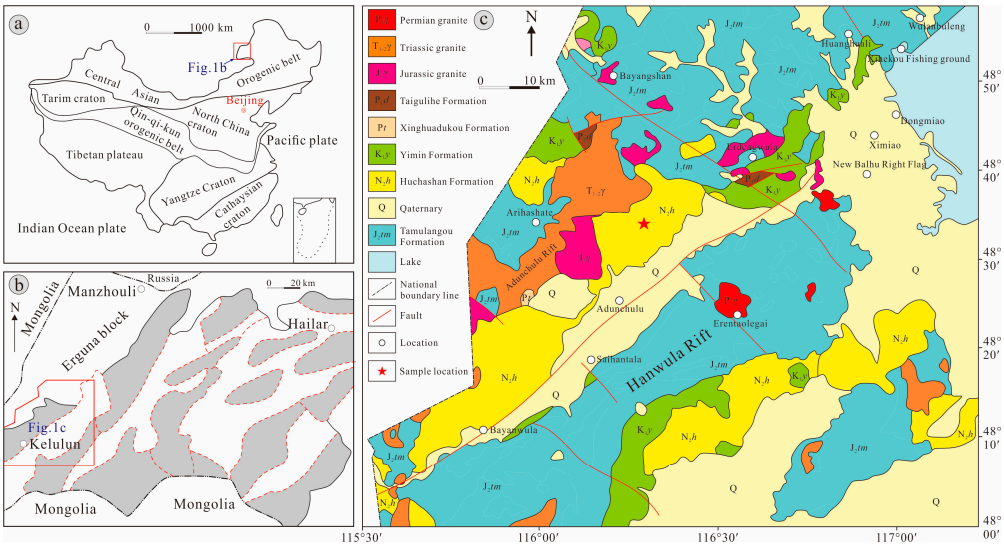

Figure 1. Regional geologic map of the Kelulun Depression in the Hailar Basin [1]. (**a**). Tectonic location map of the Hailar Basin. (**b**). Schematic diagram of structural unit division of the Hailar Basin. (**c**). Regional geological map of the Kelulun Depression.

3. Samples and Methods

Samples were collected from one borehole and from the medium-fine-grained sandstone of the Cretaceous Yimin Formation in the Kelulun Depression. Seventeen sandstone samples were collected as representative samples and subjected to further study.

3.1. Microscopic Observations

Thin sections were produced at the Langfang Geological Exploration Technology Service Co., Ltd., Guangzhou, China. Indoor microscopic petrological observations and analysis of the clastic particle composition were carried out at the Basic Geological Laboratory of East China University of Technology. The microscope used in this study was a Zeiss AxioImager M2m in order to minimize errors in the statistical analysis of the clastic particle composition. The selected sandstone samples had the following characteristics: mineral particle diameters ranging from 0.0625 to 2 mm. At least 300 grains were counted in each thin section. In addition, the percentage of cement content in the sample remained below 25 area%.

3.2. Major and Trace Element Analysis

Analysis of the major, trace, and rare earth elements was performed by ALS Chemex (Guangzhou, China) Co., Ltd. The major elements were analyzed using an XRF-1800 X-ray fluorescence spectrometer (Shimadzu Corporation, Koyto, Japan), and the analytical precision was maintained within 5%. Trace and rare earth elements were analyzed using a Thermo Fisher X Series II quadrupole plasma mass spectrometer (Waltham, MA, USA). The analytical precision was <5% for trace element contents greater than 10 ppm and <10%

for contents less than 10 ppm. The chemical analyses were performed as described by Chen (2000) [26].

3.3. Uranium Mineral Composition Analysis

Uranium mineral composition and energy spectrum analyses were performed at the State Key Laboratory of Nuclear Resources and Environment, East China University of Technology, Jiangxi Province, China. Electron probe microanalysis (EPMA) was used in the experiment. The analyzing procedure was conducted according to the national standard [27]. The standard samples used for calibration included U-UO_2, Y-yttrium aluminum, and Si-albite.

4. Results

4.1. Petrographic Characteristics

The Yimin Formation has a medium-to-fine-grained sandy texture (Figure 2a). The clasts mostly consist of quartz, feldspar (Figure 2c), and lithic fragments and minor biotite accompanied by heavy minerals, such as zircon and opaque metal minerals. The main type of support for the clastic particles is particle support, with basal-pore-type cementation between the particles. Calcareous cement is the main form (Figure 2b), although local argillaceous cement is observed. The clasts area accounts for 85–90% of the clast area, while the cement area accounts for 10–15%. The overall sorting and roundness of the mineral particles are poor, and the compositional and structural maturity are low, reflecting the close distance of the sediment transport and the characteristics of the near-source accumulation. The detrital quartz presents an angular-to-subangular shape, with grain sizes ranging from 0.13 to 0.50 mm. Quartz accounts for 35–55% of the clast area. The observed feldspar types are plagioclase, potassium feldspar, microcline, and perthite, with angular to subangular particles with grain sizes ranging from 0.11 to 0.46 mm. Plagioclase develops polysynthetic twins with strong clayification and sericitization. Several microclines are internally encrusted with altered biotite, and perthite develops strong clayification. Feldspar accounts for 10–25% of the clast area. The lithic fragments are angular-subangular, with grain sizes ranging from 0.12 to 0.53 mm, although several grains are larger than 2.00 mm. The lithic fragments mainly include granite fragments (Figure 2d) but also include small amounts of andesite fragments (Figure 2e), crystal tuff fragments (Figure 2f), and quartzite fragments. The lithic fragments account for 20–50% of the clast area. Biotite is present in a xenomorphic sheet-like shape and includes a few compacted sheets and bent crystals (Figure 2g). Some biotites exhibit strong chloritization, and iron oxides fill in or are around the cleavage joints of biotite. Biotite accounts for 2–4% of the clast area. In addition, the rocks are interspersed with pyrite (Figure 2h) and asphalt veins (Figure 2i).

4.2. Major Elements Geochemistry

The major element data for the sandstones of the Lower Cretaceous Yimin Formation in the Kelulun Depression are shown in Table 1. The SiO_2 content of the Yimin Formation (K_1y) sandstone ranges from 61.2 wt% to 76.6 wt%, the Al_2O_3 content ranges from 12.1 wt% to 15.0 wt%, the content of $Fe_2O_3{}^T$ varies greatly, ranging from 1.08 wt% to 5.41 wt%, the MgO content ranges from 0.30 wt% to 1.44 wt%, the CaO content ranges from 0.47 wt% to 2.73 wt%, the K_2O content ranges from 3.34 wt% to 4.12 wt%, and the Na_2O content ranges from 1.86 wt% to 3.44 wt%.

Table 1. Analysis results of the major elements in the sandstone samples from the study area (wt%).

Sample	HL01	HL02	HL03	HL04	HL05	HL06	HL07	HL08	HL09	HL10	HL11	HL12	HL13	HL14	HL15	HL16	HL17
SiO_2	75.4	76.6	70.0	73.5	61.2	73.2	70.5	68.8	65.5	70.2	67.7	71.6	76.2	70.5	68.8	69.3	70.7
TiO_2	0.32	0.26	0.51	0.36	0.59	0.30	0.38	0.37	0.68	0.39	0.57	0.35	0.29	0.42	0.49	0.60	0.48
Al_2O_3	12.6	12.1	14.7	12.8	14.9	12.9	14.0	13.7	15.0	13.7	14.1	13.0	12.8	14.2	13.9	14.2	13.4
$Fe_2O_3{}^T$	1.30	1.08	2.06	1.30	5.41	1.35	2.37	3.61	3.75	1.80	2.87	1.94	1.12	2.60	3.77	3.45	2.53
FeO	0.69	0.68	1.19	0.69	1.98	0.20	0.15	0.20	0.16	0.12	0.42	0.17	0.39	0.19	1.46	1.47	1.14
MnO	0.02	0.02	0.04	0.02	0.05	0.01	0.10	0.01	0.02	0.02	0.02	0.04	0.02	0.05	0.06	0.04	0.04

Table 1. *Cont.*

Sample	HL01	HL02	HL03	HL04	HL05	HL06	HL07	HL08	HL09	HL10	HL11	HL12	HL13	HL14	HL15	HL16	HL17
MgO	0.78	0.70	1.23	0.85	1.44	0.75	0.70	0.92	1.08	1.13	1.17	0.98	0.30	0.70	1.26	1.42	1.09
CaO	0.52	0.47	0.73	0.56	0.69	0.71	1.06	0.84	1.15	0.93	1.02	0.88	0.69	0.81	2.73	1.30	1.06
Na_2O	2.74	2.72	2.35	2.59	2.06	2.34	3.09	1.92	2.06	1.86	2.14	2.06	2.91	3.44	2.61	3.04	2.79
K_2O	3.73	3.70	3.93	3.80	3.80	3.67	3.98	3.98	3.60	4.12	3.68	4.04	3.97	3.70	3.34	3.57	3.66
P_2O_5	0.06	0.04	0.13	0.05	0.14	0.06	0.08	0.07	0.12	0.07	0.15	0.06	0.04	0.14	0.10	0.15	0.09
LOI	2.06	2.28	4.10	3.91	9.16	5.05	3.89	6.48	7.46	6.17	7.07	5.27	2.10	3.39	2.76	3.28	3.50
Total	99.4	100	99.8	99.7	99.3	100	100	100	100	100	100	100	100	99.9	99.8	100	100
CIA	57	56.5	60.9	57.6	62.9	58.4	55.3	59.7	61.5	59.8	60	58.1	55.2	55.9	51.9	55.8	56.1
ICV	1.01	1.00	0.99	1.01	1.13	0.96	1.09	1.06	1.03	1.00	1.06	1.05	0.96	1.07	1.39	1.26	1.16
F_1	−5.06	−5.27	−4.50	−5.24	−2.34	−4.79	−3.16	−3.64	−2.60	−5.30	−3.92	−5.15	−4.40	−2.58	−1.65	−3.10	−3.91
F_2	2.52	2.53	1.87	2.39	0.19	1.97	3.58	1.16	1.00	1.56	1.17	1.79	3.78	3.58	1.74	2.06	2.22
Al_2O_3/TiO_2	39.6	46.2	29.02	35.9	25.3	42.8	36.9	36.5	22.2	35.3	24.7	37.7	44.7	33.8	28.3	23.5	27.9
Al_2O_3/MgO	16.1	17.34	12	15.1	10.3	17.1	20	14.5	13.9	12.1	12	13.32	42.8	20.7	11	9.96	0.87
C	0.15	0.13	0.23	0.15	0.62	0.16	0.25	0.42	0.43	0.20	0.32	0.22	0.13	0.27	0.35	0.34	0.27

Chemical index of alteration (CIA) = $100Al_2O_3/(Al_2O_3 + CaO^* + Na_2O + K_2O)$ [28]. The chemical composition of the formula is the mole number, CaO* is only the CaO in silicate minerals, and because silicate is not easy to dissolve, the more accurate value of CaO in the source area is preserved. In this paper, the correction method proposed by McLennan was adopted for CIA calculation, i.e., according to the average composition of Na and Ca in natural silicate minerals and the mole ratio of CaO/Na_2O in sediment samples; if the CaO mole is greater than Na_2O, Na_2O mole is used as CaO mole, otherwise, the CaO mole is used. Index of compositional variability (ICV) = $(Fe_2O_3 + K_2O + Na_2O + CaO + MgO + MnO + TiO_2)/Al_2O_3$ [29]. $F_1 = -1.773TiO_2 + 0.607Al_2O_3 + 0.76Fe_2O_3 - 1.5MgO + 0.616CaO + 0.509 \times Na_2O - 1.224K_2O - 0.909$, $F_2 = 0.445TiO_2 + 0.07Al_2O_3 - 0.25Fe_2O_3 - 1.142MgO + 0.438CaO + 1.475Na_2O + 1.426K_2O - 6.861$ [28]. C-value = Σ(Fe + Mn + Cr + Ni + V + Co)/(Ca + Mg + Sr + Ba + K + Na) [30]. $Fe_2O_3{}^T$ refer to total iron.

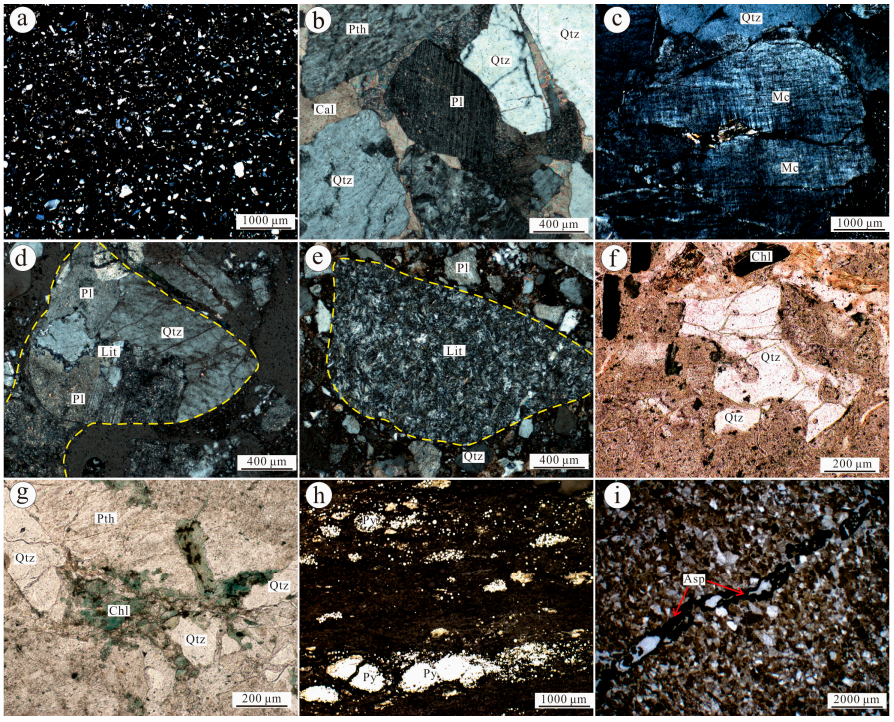

Figure 2. Petrographic characteristics of the Yimin Formation sandstone in the Kelulun Depression. (**a**) Medium-fine-grained sand structure. (**b**) Plagioclase with polylamellar twin-crystals, the surface is weakly sericite. (**c**) Microplagioclase develops lattice twinning. (**d**) Granite detritus. (**e**) Andesite detritus. (**f**) Tuff detritus, dissolution of estuarine quartz. (**g**) Biotite; (**h**) Framboidal pyrite. (**i**) Bituminous veins. Qtz: Quartz. Pl: Plagioclase. Pth: Perthite. Mc: Microcline. Py: Pyrite. Lit: Lithic. Chl: Chlorite. Asp: Bituminous. Cal: Calcite.

4.3. Trace and Rare Earth Elements Geochemistry

The trace and rare earth elements (REE) data for the sandstones are listed in Table 2. In the spider diagram of trace elements, all samples present similar trends, the abundance of trace elements is slightly lower than that in the upper continental crust, and the characteristics are rich in U, Th, and Rb and poor in Sr, Cr, Ni, Be, Mo, Zr, and Hf (Figure 3). A few

samples are richer in U and Mo, because six samples are collected in the mineralized section, and the content of U is high. However, U and Mo have similar geochemical characteristics, so the trend of U and Mo is different from other samples.

Table 2. Trace and REE elements analysis results for sandstones from the study area (ppm).

Sample	HL01	HL02	HL03	HL04	HL05	HL06	HL07	HL08	HL09	HL10	HL11	HL12	HL13	HL14	HL15	HL16	HL17
Li	11.9	11.0	30.6	14.8	44.5	7.94	9.95	8.58	16.3	9.24	8.71	12.6	12.1	11.7	14.0	18.8	20.2
Be	1.61	1.73	2.29	2.03	2.85	1.47	1.93	2.77	2.56	2.01	2.38	2.04	1.69	1.94	2.15	1.93	1.92
Sc	3.92	3.12	7.36	3.93	9.18	3.70	5.48	5.22	8.80	5.36	6.58	4.71	3.70	5.25	8.64	7.59	6.79
V	28.5	24.0	75.1	103	80.9	29.8	42.1	52.0	56.5	38.3	56.5	31.0	30.7	36.3	77.2	68.7	51.4
Cr	10.5	7.39	21.3	12.7	29.8	7.71	8.82	11.4	18.8	14.0	14.9	8.96	6.00	11.7	13.4	18.4	14.1
Mn	152	132	313	156	360	94.7	740	102	181	145	193	292	126	346	436	317	279
Co	4.10	3.32	6.19	4.24	12.3	3.60	5.16	4.84	7.72	4.81	6.06	3.41	2.14	4.85	7.71	8.63	6.62
Ni	6.93	5.55	9.12	6.55	16.3	7.52	7.42	8.55	14.4	10.3	9.07	6.80	3.64	8.09	8.91	14.6	7.88
Cu	6.37	5.17	20.4	5.11	32.2	7.44	10.1	15.0	22.9	12.9	18.9	12.6	7.50	10.9	8.09	12.2	11.0
Zn	65.2	53.2	87.6	42.7	91.5	41.1	44.7	47.2	70.8	56.8	42.1	80.0	48.7	46.3	64.4	83.4	62.4
Ga	12.8	11.4	17.5	13.2	18.7	12.1	14.1	13.5	16.8	13.7	15.7	14.3	11.9	16.5	16.1	15.3	15.1
Rb	138	134	157	138	157	129	127	154	138	157	126	155	129	122	122	123	129
Sr	169	165	168	158	145	187	226	197	230	207	208	152	159	210	268	234	197
Y	11.0	9.58	23.2	16.0	21.4	11.6	16.6	13.1	23.2	14.5	18.2	13.6	14.2	16.1	22.0	20.3	19.2
Zr	56.2	39.7	106	67.7	128	46.6	64.5	52.1	103	53.6	83.5	80.8	50.4	76.5	66.6	148	79.7
Nb	8.72	7.14	12.1	9.04	12.6	7.17	9.05	7.98	12.2	9.37	11.7	9.42	8.18	8.25	9.55	10.1	10.7
Mo	16.3	19.0	0.46	7.50	15.0	0.31	0.45	0.45	0.27	0.26	0.23	0.34	0.25	0.61	0.30	0.59	0.73
Ag	0.08	0.07	0.32	0.08	0.39	0.11	0.13	0.11	0.13	0.12	0.11	0.28	0.10	0.14	0.35	0.14	0.30
Cd	0.13	0.10	3.56	0.09	0.93	0.02	0.08	0.06	0.07	0.05	0.14	0.05	0.05	0.05	0.23	0.12	0.21
In	0.04	0.04	0.08	0.04	0.1	0.03	0.06	0.04	0.06	0.05	0.05	0.06	0.05	0.05	0.07	0.06	0.06
Sn	1.41	1.14	2.68	1.50	2.73	1.11	1.91	1.54	2.34	1.90	2.06	1.78	1.24	2.28	2.80	1.87	2.15
Sb	1.33	0.74	0.37	0.57	3.24	0.19	0.26	0.31	0.44	0.39	0.31	0.41	0.32	0.26	4.03	0.73	0.48
Cs	4.91	4.20	8.23	5.30	9.70	4.59	3.68	6.11	7.10	6.40	5.56	5.82	4.44	4.46	3.75	5.68	5.16
Ba	405	397	469	420	429	429	541	391	388	415	413	469	501	682	446	453	483
Hf	2.25	1.68	3.86	2.63	4.80	1.93	2.53	2.14	4.38	2.27	3.74	3.06	1.89	2.57	2.46	4.00	2.96
Ta	1.91	1.38	1.96	1.46	2.19	1.25	1.24	1.07	1.80	1.43	1.64	1.36	1.34	1.13	1.44	1.28	1.51
W	1.25	0.88	1.79	1.25	2.57	1.31	1.27	2.05	2.17	1.72	1.34	1.51	1.34	4.49	2.32	1.36	2.83
Re	0	0.02	0	0.04	0.04	0	0	0	0.02	0	0	0	0	0	0	0	0.02
Tl	0.74	0.74	0.98	0.80	1.14	0.76	0.82	0.87	0.8	0.9	0.72	0.98	0.88	0.77	0.81	0.77	0.86
Pb	19.8	16.7	96.0	18.0	130	14.8	19.0	25.0	33.3	24.2	25.9	29.2	23.6	25.0	24.7	25.8	22.6
Bi	0.32	0.61	0.97	0.21	1.51	0.35	0.54	0.70	0.99	0.72	0.85	0.62	0.28	0.52	0.93	0.93	0.40
Th	7.91	6.92	22.3	8.40	32.5	8.39	13.9	11.1	16.8	11.4	15.4	14.2	6.63	13.1	13.8	11.7	12.4
U	41.0	36.2	59.1	58.4	89.3	4.19	4.38	3.15	5.32	3.40	9.18	4.41	2.62	3.12	5.53	4.85	21.4
La	25.1	19.4	39.2	28.6	46.3	21.6	26.3	23.1	29.9	21.2	35.5	33.2	19.8	43.3	27.9	29.1	34.0
Ce	55.9	40.5	69.7	54.3	79.7	35.4	43.4	48.3	65.5	40.8	72.1	61.5	34.7	81.7	55.1	62.2	68.2
Pr	5.39	4.30	9.29	6.28	9.71	4.95	5.69	5.15	7.03	4.95	8.33	7.20	4.64	9.31	6.48	6.92	7.70
Nd	18.8	15.0	33.4	22.5	34.1	17.8	20.2	17.9	25.6	17.6	29.9	25.6	16.6	32.3	23.7	25.9	27.6
Sm	3.14	2.51	6.01	3.76	5.69	3.14	3.56	3.14	4.74	3.19	5.10	4.20	2.99	5.33	4.50	4.71	4.80
Eu	0.60	0.51	1.11	0.77	0.96	0.65	0.86	0.60	0.89	0.64	0.90	0.78	0.67	1.13	1.00	1.08	0.95
Gd	2.41	1.93	4.96	2.99	4.68	2.46	2.94	2.55	4.18	2.63	4.01	3.15	2.40	4.15	3.95	3.96	3.97
Tb	0.34	0.28	0.75	0.45	0.67	0.36	0.45	0.40	0.65	0.41	0.56	0.43	0.37	0.56	0.63	0.61	0.60
Dy	1.68	1.47	4.06	2.55	3.49	1.81	2.48	2.14	3.73	2.20	2.93	2.18	2.01	2.79	3.51	3.35	3.26
Ho	0.32	0.26	0.80	0.50	0.71	0.34	0.51	0.42	0.74	0.43	0.57	0.45	0.40	0.51	0.69	0.67	0.63
Er	0.93	0.76	2.32	1.51	1.98	0.98	1.46	1.25	2.23	1.31	1.73	1.24	1.16	1.45	2.04	2.00	1.84
Tm	0.16	0.13	0.36	0.25	0.30	0.16	0.24	0.21	0.37	0.21	0.28	0.20	0.24	0.23	0.32	0.32	0.29
Yb	1.06	0.89	2.46	1.63	2.01	1.07	1.61	1.50	2.52	1.44	1.91	1.41	1.31	1.53	2.15	2.08	1.96
Lu	0.16	0.14	0.38	0.25	0.32	0.17	0.25	0.23	0.40	0.23	0.29	0.21	0.20	0.23	0.34	0.32	0.30
Y	11.0	9.58	23.2	16.0	21.4	11.6	16.6	13.1	23.2	14.5	18.2	13.6	14.2	16.1	22.0	20.3	19.2
ΣREE	116	88.2	174	126	190	90.9	110	107	149	97.3	164	142	87.5	185	132	143	156
LREE	109	82.3	159	116	176	83.5	99.9	98.2	134	88.4	152	132	79.4	173	119	130	143
HREE	7.05	5.87	16.1	10.1	14.2	7.35	9.94	8.70	14.8	8.86	12.3	9.27	8.09	11.5	13.6	13.3	12.9
LREE/HREE	15.5	14.0	9.86	11.5	12.5	11.4	10.1	11.3	9.03	10.0	12.4	14.3	9.81	15.1	8.70	9.76	11.1
La_N/Yb_N	17	15.7	11.4	12.6	16.5	14.5	11.7	11.0	8.52	10.6	13.3	16.8	10.9	20.3	9.29	10	12.4
δEu	0.66	0.7	0.62	0.71	0.57	0.71	0.81	0.65	0.61	0.7	0.61	0.65	0.76	0.73	0.73	0.76	0.67
δCe	1.18	1.09	0.90	0.99	0.92	0.84	0.87	1.09	1.11	0.98	1.03	0.98	0.89	1.00	1.00	1.07	1.03
La/Sc	6.40	6.23	5.33	7.26	5.04	5.84	4.80	4.41	3.40	3.97	5.40	7.04	5.35	8.25	3.23	3.83	11.7
Th/Sc	2.02	2.22	3.03	2.14	3.54	2.27	2.53	2.12	1.91	2.12	2.34	3.02	1.79	2.49	1.60	1.54	12.4
La/Co	6.12	5.85	6.34	6.73	3.76	6.00	5.09	4.76	3.88	4.41	5.85	9.74	9.24	8.94	3.62	3.37	1.87
Th/Co	1.93	2.08	3.61	1.98	2.65	2.33	2.69	2.29	2.17	2.36	2.54	4.18	3.09	2.70	1.80	1.35	1.14
Sr/Cu	26.5	31.9	8.23	30.9	4.51	25.2	22.3	13.2	10.1	16.1	11.0	12.0	21.2	19.4	33.1	19.1	31.7
U/Th	5.18	5.23	2.65	6.95	2.74	0.50	0.32	0.28	0.32	0.30	0.60	0.31	0.39	0.24	0.40	0.41	3.64
V/Cr	2.73	3.25	3.53	8.14	2.72	3.86	4.78	4.56	3.01	2.73	3.79	3.46	5.11	3.09	5.76	3.74	1.19
Ni/Co	1.69	1.67	1.47	1.54	1.32	2.09	1.44	1.77	1.87	2.13	1.50	2.00	1.70	1.67	1.16	1.69	0.87
V/(V + Ni)	0.80	0.81	0.89	0.94	0.83	0.80	0.85	0.86	0.80	0.79	0.86	0.82	0.89	0.82	0.90	0.82	0.87
Rb/Sr	0.82	0.82	0.93	0.88	1.08	0.69	0.56	0.78	0.60	0.76	0.61	1.02	0.81	0.58	0.46	0.53	0.66

LREE = La + Ce + Pr + Nd + Sm + Eu, HREE = Gd + Tb + Dy + Ho + Er + Tm + Yb + Lu. $\delta Eu = 2Ce_{CN}/(La_{CN} + Pr_{CN})$, $\delta Ce = 2Eu_{CN}/(Sm_{CN} + Gd_{CN})$. N is standard for chondrite.

The total content of REE (ΣREE) of the Yimin Formation sandstone ranges from 87.5 ppm to 190 ppm, while the ratio of LREE/HREE varies between 8.7 and 15.5 (Table 2). The chondrite-normalized REE patterns are right-sloping with moderately negative Eu

anomalies (Figure 4a). The normalized REE distribution curve for the upper continental crust (UCC) is gently sloped (Figure 4b), suggesting that the REE composition is comparable to that in the UCC. This indicates that the sandstones originated from the UCC [31].

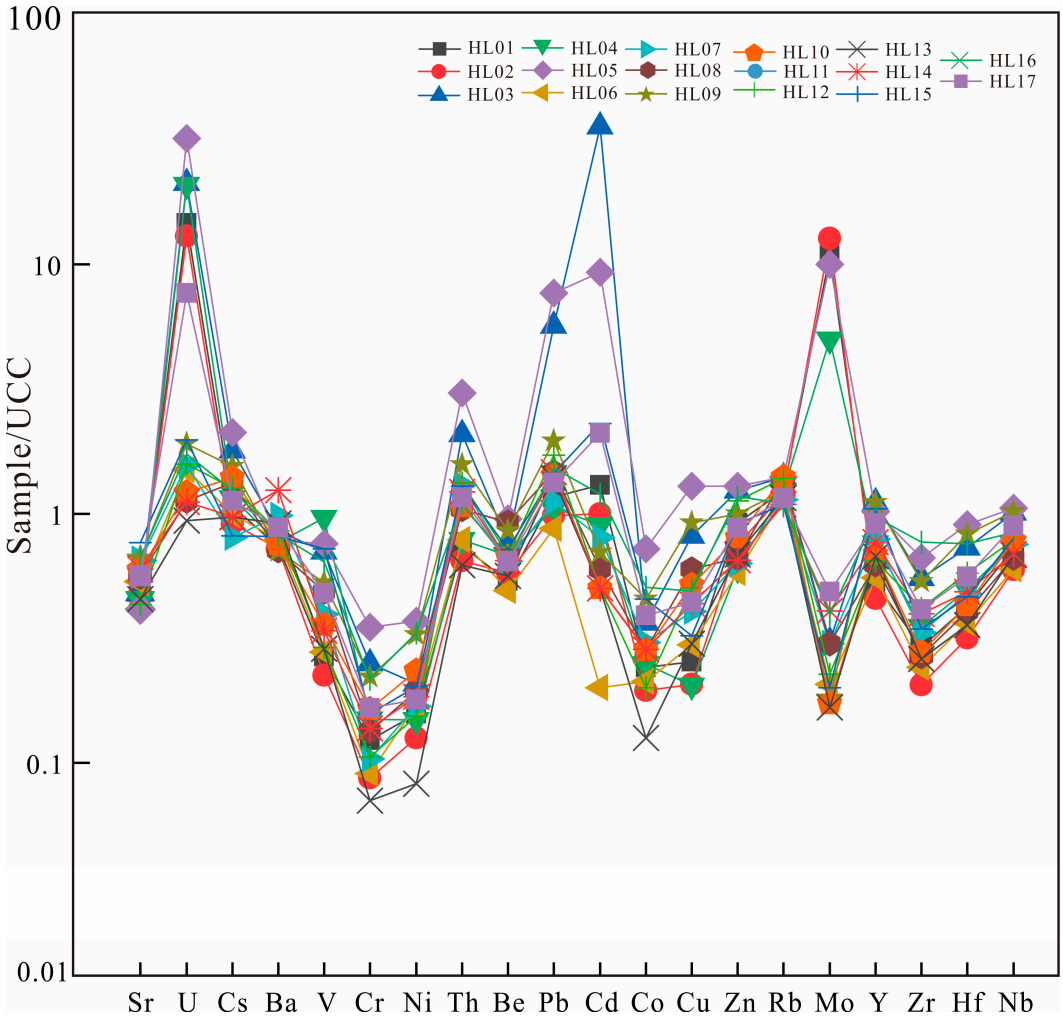

Figure 3. UCC-normalized [32] trace element spider diagram of the Yimin Formation sandstone, Kelulun Depression.

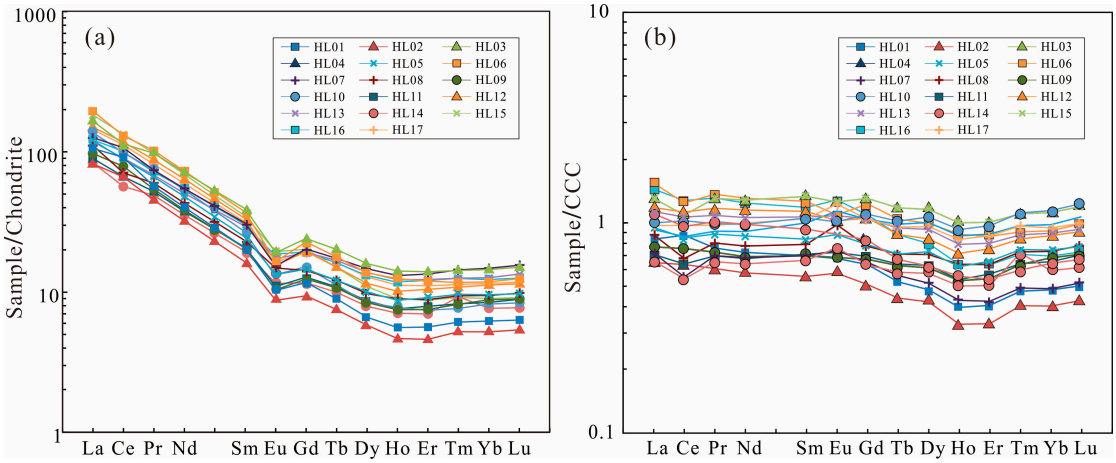

Figure 4. Chondrite-normalized REE patterns [33] (**a**) and UCC-normalized REE patterns (**b**) of the Yimin Formation sandstone, Kelulun Depression [32].

4.4. Uranium Mineralogy and Mineral Chemistry

The EPMA results presented in Table 3 indicate that coffinite ($U(SiO_4)_{1-x}(OH)_{4x}$) and uranium-titanium oxides are the major uranium minerals in the studied sandstones.

Table 3. EPMA results of uranium minerals from sandstone samples from the Yimin Formation in the Kelulun Depression (wt%).

Coffinite											
Comment	**SiO_2**	**Al_2O_3**	**Y_2O_3**	**BeO**	**CaO**	**TiO_2**	**ZrO_2**	**FeO**	**UO_2**	**P_2O_5**	**Total**
1	16.92	0.31	2.90	0.02	1.36	0.31	0.11	1.46	57.40	5.36	86.14
T	17.29	0.27	2.88	0.00	1.32	0.28	0.00	1.34	60.47	5.87	89.71
3	19.50	0.70	2.46	0.06	0.81	0.29	0.03	0.39	57.07	6.29	87.60
4	14.81	0.34	3.36	0.25	1.49	0.23	0.18	2.42	60.30	5.32	88.70
5	14.50	0.31	3.33	0.00	1.43	0.22	0.17	2.78	58.90	4.85	86.49
6	15.10	0.54	3.24	0.00	1.45	0.21	0.54	2.61	59.20	5.36	88.24
7	13.66	0.34	3.18	0.00	1.54	0.18	0.44	0.93	62.02	4.57	86.88
8	13.63	0.32	2.95	0.00	1.59	0.18	0.12	0.98	62.15	4.58	86.50
9	13.61	0.28	3.44	0.16	1.56	0.12	0.32	2.29	59.94	4.83	86.54
10	13.55	0.27	3.50	0.00	1.49	0.12	0.71	2.32	60.41	4.99	87.36
11	14.36	0.38	3.05	0.00	1.25	0.18	0.44	1.25	62.93	4.34	88.16
12	14.25	0.33	3.06	0.34	1.30	0.14	0.72	1.17	63.73	4.35	89.39
13	15.77	0.29	2.84	0.00	1.25	0.15	0.84	1.23	58.91	4.72	85.99
14	17.24	0.42	2.89	0.00	1.34	0.19	0.34	1.42	59.65	5.87	89.34
15	12.67	0.30	2.93	0.00	1.89	0.21	1.28	0.85	63.61	4.42	88.15
16	13.42	0.37	3.51	0.00	1.30	0.17	2.54	0.64	61.82	4.27	88.05
Uranium-titanium oxide											
Comment	SiO_2	Al_2O_3	Y_2O_3	BeO	CaO	TiO_2	ZrO_2	FeO	UO_2	P_2O_5	Total
17	11.18	1.24	0.84	1.29	0.72	43.55	0.68	1.07	31.94	0.04	92.55
18	10.69	1.88	0.20	1.80	2.16	36.36	0.72	1.70	36.11	0.08	91.71
19	11.81	0.30	0.01	1.15	0.31	39.88	0.77	2.22	33.46	0.06	89.95
20	8.80	1.03	0.65	1.27	1.36	38.46	0.71	2.16	34.51	0.05	88.98
21	8.70	0.47	0.40	2.57	1.93	41.96	1.26	2.16	36.92	0.04	96.40
22	10.88	1.16	0.42	1.77	2.00	40.82	1.20	2.15	37.04	0.00	97.44
23	11.18	1.24	0.84	1.29	0.72	43.55	0.68	1.07	31.94	0.05	92.56

The UO_2 content in coffinite ranges from 57.1 wt% to 63.7 wt%, the SiO_2 content ranges from 12.7 wt% to 19.5 wt%, the CaO content ranges from 0.81 wt% to 1.89 wt%, the content of P_2O_5 ranges from 4.27 wt% to 6.29 wt%, the Y_2O_3 content ranges from 2.46 wt% to 3.51 wt%, and FeO, TiO_2, and Al_2O_3 are found in small amounts. A coffinite chemical formula based on the averaged EPMA results in Table 3 is $Si_{0.07}U_{0.534}Ca_{0.01}P_{0.022}Ti_{0.01}Fe_{0.01}Y_{0.02}O_4$.

The UO_2 content in uranium-titanium oxide ranges from 31.9 wt% to 37.1 wt%, the TiO_2 content ranges from 36.4 wt% to 43.6 wt%, the SiO_2 content ranges from 8.70 wt% to 11.81 wt%, the CaO content ranges from 0.31 wt% to 2.16 wt%, the BeO content ranges from 1.15 wt% to 2.57 wt%, and FeO, P_2O_5, Y_2O_3, Al_2O_3, ZrO_2, and MgO are found in small amounts.

The BSE micrographs of the studied uranium minerals (Figure 5) show that the average particle size of coffinite and uranium-titanium oxide ranges from 1 to 5 μm. Based on the characteristics of the uranium mineral morphology and assemblage, the following classes are identified:

(1) Coffinite distributed in an irregular granular or colloidal form within framboidal pyrite (Figure 5a) or between submicron cubic pyrite crystals (Figure 5b), and coffinite tightly cemented with framboidal pyrite (Figure 5c);
(2) Coffinite distributed in stellate and micro-vein forms at the edges, cracks, or dissolution pits of detrital quartz, potassium feldspar, and biotite (Figure 5d–f);

(3) Coffinite and uranium-titanium oxide in colloidal (Figure 5g), burr-like, or micro-columnar shapes around pyrite (Figure 5h) and anatase (Figure 5i), thus forming assemblages of chlorite-pyrite-coffinite and chlorite-anatase-uranium titanium oxide.

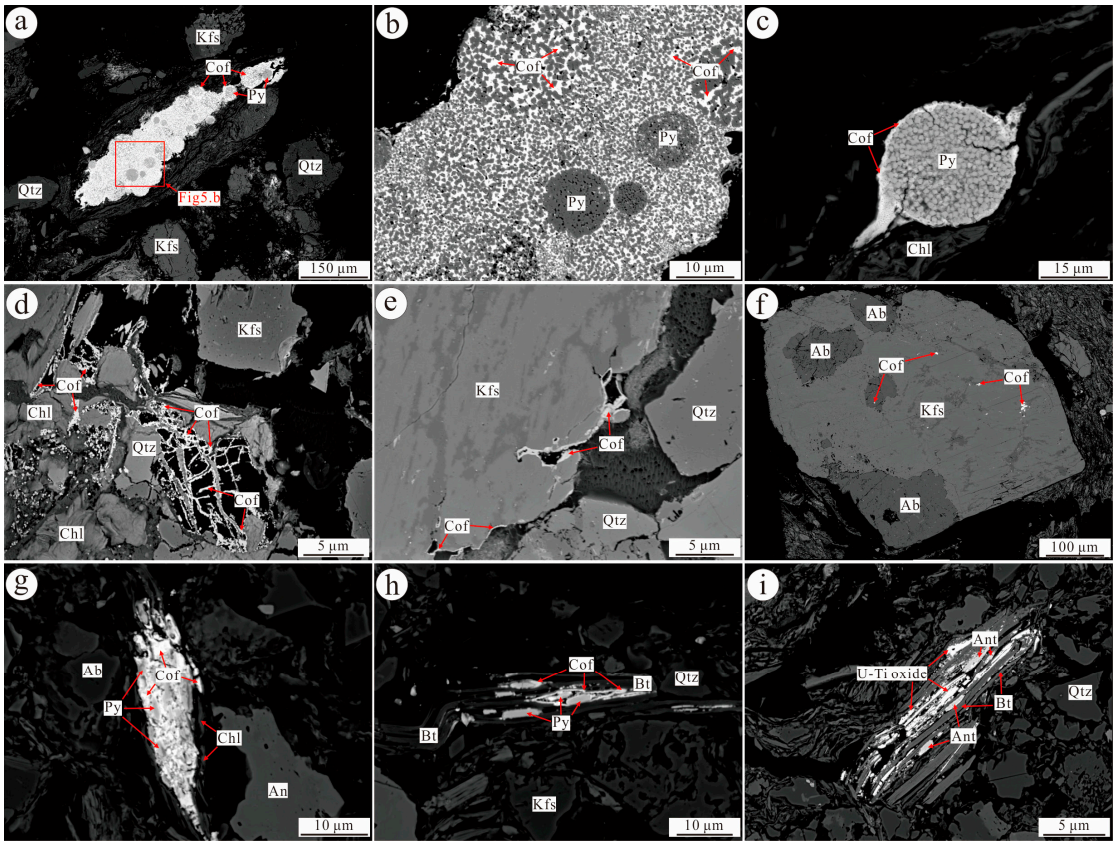

Figure 5. BSE micrographs of uranium minerals from the Yimin Formation sandstone in the Kelulun Depression. (**a**) Coffinite between framboidal pyrite aggregates. (**b**) Local magnification of Figure (**a**). (**c**) Coffinite surrounds the rim of pyrite. (**d**) Coffinite is distributed along the edges of clastic quartz and feldspar micro-veins. (**e**) Coffinite distributed in the margin of clastic quartz. (**f**) Coffinite distributed in the dissolution pores of potassium feldspar. (**g**) Chlorite-pyrite-coffinite. (**h**) Biotite-pyrite-coffinite. (**i**) Chlorite-anatase-titanium-uranium oxide. Cof: Coffinite. U-Ti oxide: Uranium titanium oxide. Qtz-Quartz. Kfs: Potassium feldspar. Ab: Albite. An: Anorthite. Bt: Biotite. Ant: Anatase. Chl: Chlorite. Py: Pyrite.

5. Discussion

5.1. Provenance

The trace elements (including REEs) of fine-grained clastic rocks are relatively stable in the later diagenesis and weathering processes, thus making them reliable tools for tracing the provenances and depositional settings of other elements [34,35].

The Al_2O_3/TiO_2 ratio in the mafic igneous rock source is less than 8, the Al_2O_3/TiO_2 ratio in the intermediate igneous rock source ranges from 8 to 21, and the Al_2O_3/TiO_2 ratio in the felsic igneous rock source is greater than 21 [36]. The Al_2O_3/TiO_2 ratio of the Yimin Formation ranges from 22.2 to 46.2 (Table 1), indicating that the source rocks of the Yimin Formation sandstone are felsic igneous rocks. In the TiO_2-Al_2O_3 diagram (Figure 6a), the samples are located in the granite and granodiorite region. In the F_2-F_1 diagram (Figure 6b), all samples plot in the source area of the felsic igneous provenance. Similarly, in the K_2O-Rb diagram, the samples plot in the felsic intermediate region (Figure 6c), while in the TiO_2-Ni diagram, the Yimin Formation sandstones plot in the felsic source area (Figure 6d), indicating that the source rocks of the Yimin Formation sandstone are felsic rocks.

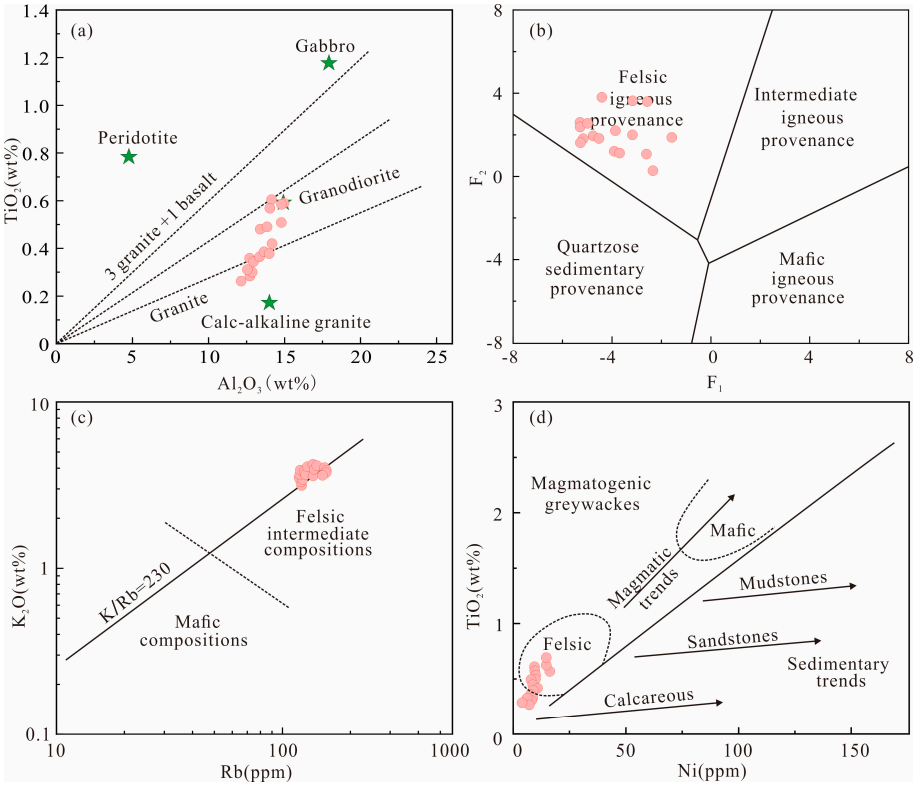

Figure 6. (**a**) TiO_2-Al_2O_3 [37], (**b**) F_2-F_1 [28], (**c**) K_2O-Rb [38], and (**d**) TiO_2-Ni [39] diagrams for the Yimin Formation.

The Co/Th-La/Sc (Figure 7a), Ti/Zr-La/Sc (Figure 7b), La/Th-Hf (Figure 7c), Th/Sc-Zr/Sc (Figure 7d), La-Th-Sc (Figure 8a), Th-Hf-Co (Figure 8b), and V-Ni-Th×10 (Figure 8c) results show that the source rocks of the Yimin Formation are mainly felsic rocks, and in particular felsic volcanic rocks.

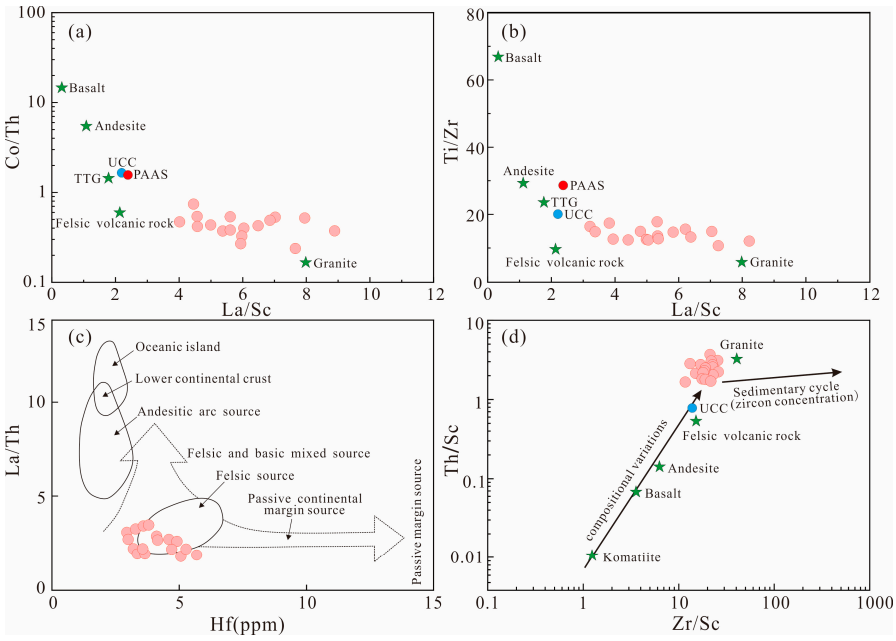

Figure 7. (**a**) Co/Th-La/Sc [40], (**b**) Ti/Zr-La/Sc [41], (**c**) La/Th-Hf [42], and (**d**) Th/Sc-Zr/Sc [43] diagrams of the Yimin Formation sandstone. UCC: Upper continental crust. PAAS: Post-archean Australian shale. TTG: Trondhjemite-tonalite-granodiorite.

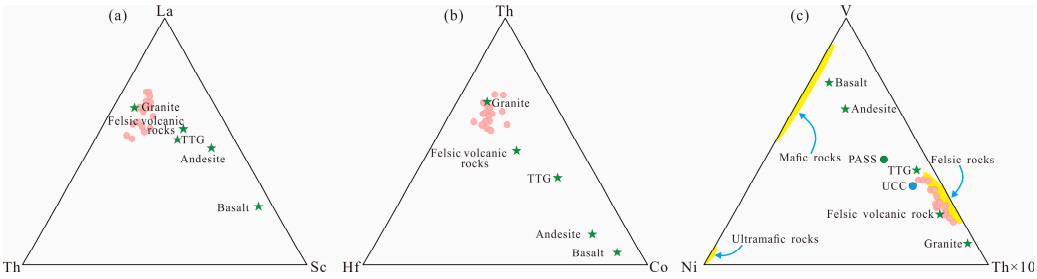

Figure 8. Source discrimination diagrams of (**a**) La-Th-Sc [44], (**b**) Th-Hf-Co [45], and (**c**) V-Ni-Th×10 [46]. UCC: Ppper continental crust. PAAS: Post-archean Australian shale. TTG: Trondhjemite-tonalite-granodiorite.

5.2. Analysis of Tectonic Setting in Provenance

Based on the major elements, trace elements, and REEs, four major tectonic setting are distinguished for sandstones [47,48]: oceanic island arc (OIA), continental island arc (CIA), active continental margin (ACM), and passive continental margin (PCM). According to the SiO_2/Al_2O_3-K_2O/Na_2O diagram (Figure 9a), $Al_2O_3/(Na_2O+CaO)$-($Fe_2O_3{}^T$ + MgO) diagram (Figure 9b), K_2O/Na_2O-($Fe_2O_3{}^T$ + MgO) diagram (Figure 9c), and SiO_2/Al_2O_3-$K_2O/(Na_2O + CaO)$ diagram (Figure 9d), the samples fall mainly within the PCM regions or on the border between the PCM and ACM regions. In the La-Th-Sc diagram (Figure 10a), the Yimin Formation samples all fall in the ACM and PCM region. In the Th-Sc-Zr/10 (Figure 10b) and Th-Co-Zr/10 diagrams (Figure 10c), the samples mainly fall in the PCM region.

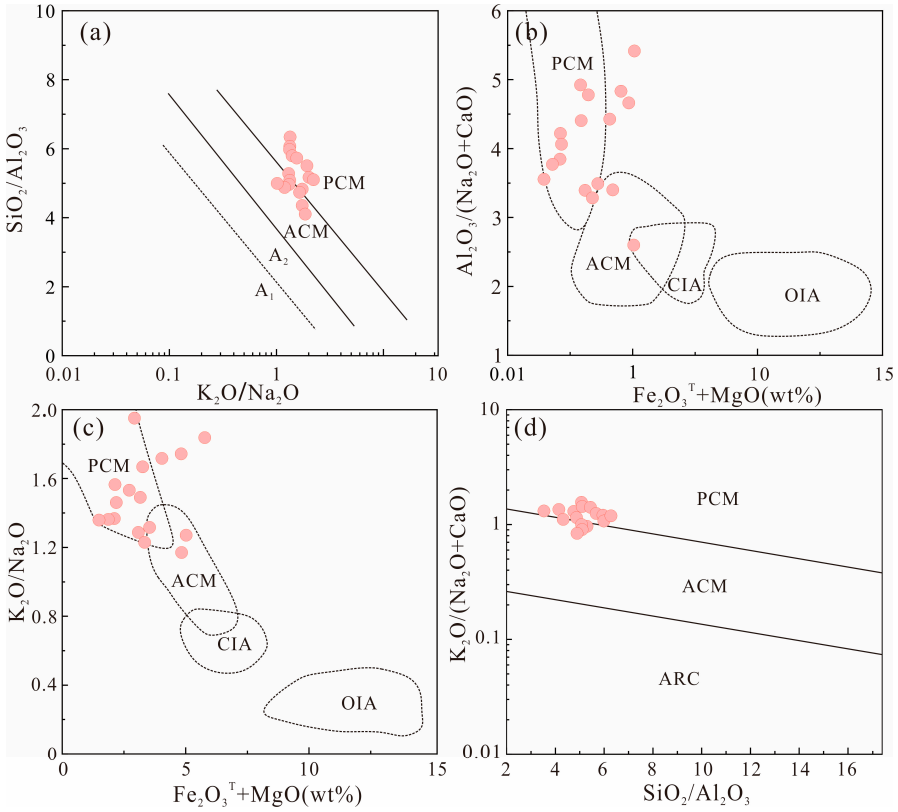

Figure 9. Trace element ternary diagrams of the tectonic setting discrimination for the Yimin Formation sandstone. (**a**) SiO_2/Al_2O_3-K_2O/Na_2O diagram [49]. (**b**) $Al_2O_3/(Na_2O + CaO)$-($Fe_2O_3{}^T$ + MgO) diagram [50]. (**c**) K_2O/Na_2O-($Fe_2O_3{}^T$ + MgO) diagram [51]. (**d**) SiO_2/Al_2O_3-$K_2O/(Na_2O + CaO)$ diagram [52]. PCM, passive continental margin. ACM, active continental margin. ARC, oceanic island arc margin. A_1, arc setting, basaltic and andesitic detritus. A_2, evolved arc setting, felsitic-plutonic detritus. OIA, oceanic island arc. CIA, continental island arc.

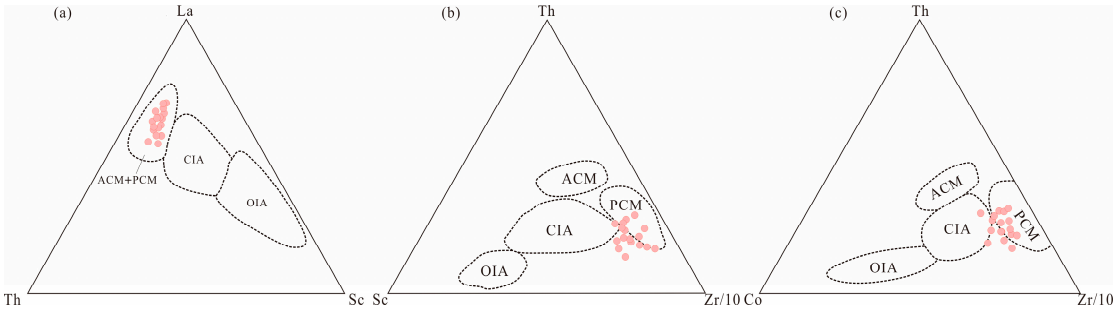

Figure 10. Diagrams of the tectonic setting discrimination for the Yimin Formation sandstone [41]. PCM, passive continental margin. ACM, active continental margin. OIA, oceanic island arc. CIA, continental island arc. (**a**) La-Th-Sc diagram. (**b**) Th-Sc-Zr/10 diagram. (**c**) Th-Co-Zr/10 diagram.

In summary, the source rocks of the Yimin Formation sandstone in the Kelulun Depression mainly formed in a passive continental margin (PCM) setting.

5.3. Redox Conditions

When using trace elements to define the redox environment of ancient sedimentary water media, the selected sample must not have been subjected to late fluid transformations [53]. The correlations between Hf and the elements Co, Ni, Cr, and Cu show linear dependences with $R^2 > 0.5$ (Figure 11), indicating that the samples represent the paleoenvironmental characteristics of the source area.

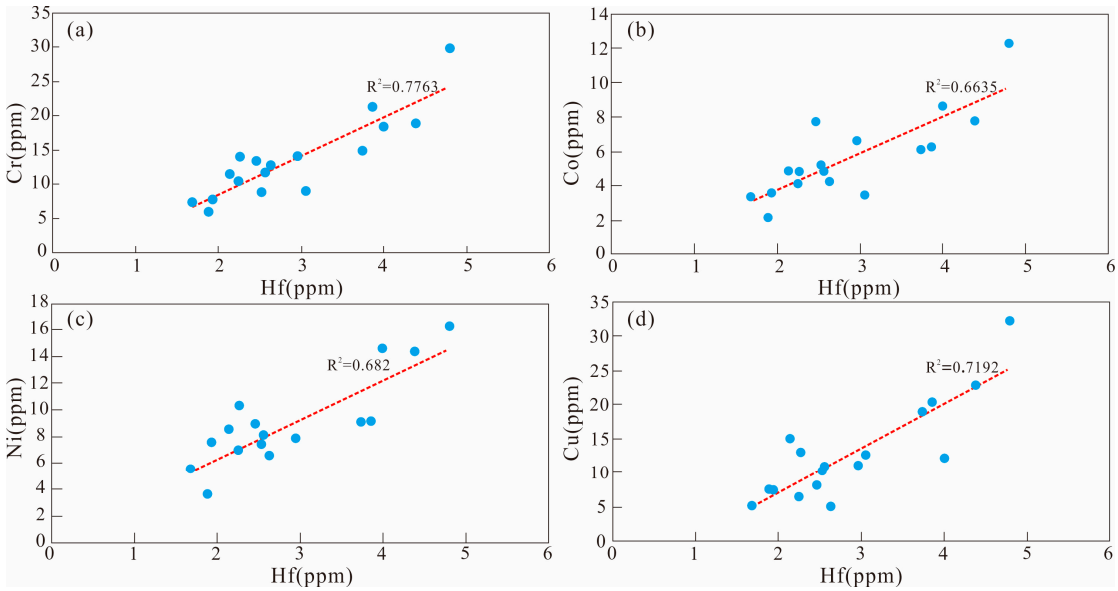

Figure 11. Correlation diagram of the contents of Co, Ni, Cr, Cu, and Hf. (**a**) Cr-Hf relational diagram. (**b**) Co-Hf relational diagram. (**c**) Ni-Hf relational diagram. (**d**) Cu-Hf relational diagram.

The contents and ratios of the redox-sensitive trace elements Mo, U, Th, Co, V, Ni, Cr, and Cu can be used to determine the redox properties of paleo-sedimentary water bodies [54]. Metals such as Ni, Cu, and Zn often exist in the form of sulfides under anoxic conditions, which also have a certain indicative significance for water bodies [55]. Therefore, the Mo, U/Th, V/Cr, Ni/Co, and V/(V + Ni) ratios are the most reliable parameters for investigating redox environments [56].

The U/Th ratio can be applied to deduce the redox conditions for the bottom waters at the boundary between water and sediment. U/Th > 1.25 indicates strongly reducing conditions, U/Th ratios between 0.75 and 1.25 indicate reducing conditions, and U/Th < 0.75 indicates oxidizing conditions [57,58]. The U/Th ratio of the Yimin Formation

sandstone ranges from 0.24 to 6.95, with most values ranging between 0.24 and 0.60, indicating that the sedimentary water bodies were all oxygen-rich (Figure 12). The sudden increase in U/Th values indicates that the degree of oxygenation of the paleowater body in this layer changed abruptly. It is speculated that uranium-rich water has a significant impact on the U/Th values within the ore-bearing layer of the Yimin Formation.

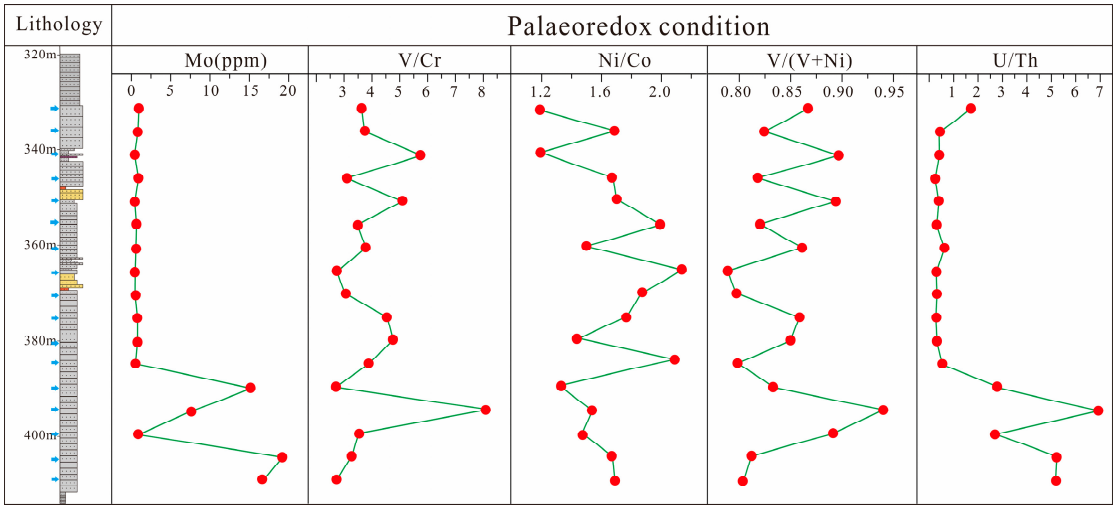

Figure 12. Diagram of discrimination of redox environment in the paleo-water body of the Yimin Formation.

Previous studies have shown that oxidized water occurs when the Mo content is less than 25 ppm and reduced water occurs when the Mo content is more than 25 ppm [59]. The Mo content of the Yimin Formation ranges from 0.23 ppm to 19 ppm, with most values ranging between 0.20 and 0.60, indicating that the Yimin Formation was deposited in an oxidizing water environment. V/Cr and Ni/Co ratios can also be used to determine the redox environment of paleo-water bodies. V/Cr < 2.0 signifies an oxygen-saturated environment, 2 < V/Cr < 4.25 denotes an oxygen-undersaturated environment, and V/Cr > 4.25 implies an anoxic environment [58,60]. The V/Cr value of the Yimin Formation ranges from 2.72 to 8.14, indicating an oxygen-undersaturated environment (Figure 12). Ni/Co < 5.00 indicates an oxygen-saturated environment, between 5.00 and 7.00 indicates an oxygen-undersaturated environment, and >7.00 implies a reduced environment [58,61]. The Ni/Co value of the Yimin Formation ranges from 1.16 to 2.13, indicating that the Yimin Formation was deposited in an oxygen-saturated environment.

The V/(V + Ni) value can help determine the intensity of the bottom water body stratification during deposition [58]. A V/(V + Ni) ratio between 0.4 and 0.6 indicates weak stratification, a ratio between 0.6 and 0.84 implies moderate stratification, and a ratio above 0.84 denotes intense stratification. The V/(V + Ni) values of the Yimin Formation sandstone in the study area range from 0.79 to 0.94, indicating that, during Early Cretaceous sedimentation, the bottom water was mainly moderately stratified and the water bodies were in an oxygen-saturated-to-undersaturated environment.

5.4. Paleoclimate Reconstruction

5.4.1. Geochemical Discriminators of Paleoclimate

The C value is a favorable indicator of paleoclimate that can reflect arid or humid conditions: Ca, Mg, Sr, Ba, K, and Na are usually enriched under dry, arid conditions, whereas Fe, Mn, Cr, Ni, V, and Co are enriched under humid conditions [61]. When the C value is greater than 0.8, from 0.6 to 0.8, from 0.4 to 0.6, 0.2 to 0.4, and less than 0.2, a humid, semi-humid, semi-humid-semi-arid, semi-arid, and arid environment is reflected, respectively [62]. The samples from the Yimin Formation have C values from 0.13 to 0.62, indicating that they were formed in an arid environment.

The ratios of Sr/Cu, Rb/Sr, and Al_2O_3/MgO in sediments can also serve as important indicators of paleoclimates. Since Sr is enriched under arid conditions, while Cu is enriched under humid conditions, Sr/Cu values ranging from 1.3 to 5.0 indicate a warm and humid climate, and values greater than 5.0 indicate an arid climate [63]. The Sr/Cu ratio of the Yimin Formation sandstone ranges from 4.51 to 42.34, with most values ranging between 15 and 30, indicating that the Yimin Formation was formed in an arid environment. The changes in the Rb/Sr and Al_2O_3/MgO ratios are similar to the changes in the C value (Figure 13), indicating that the Yimin Formation was generally in an arid environment during the sedimentary period.

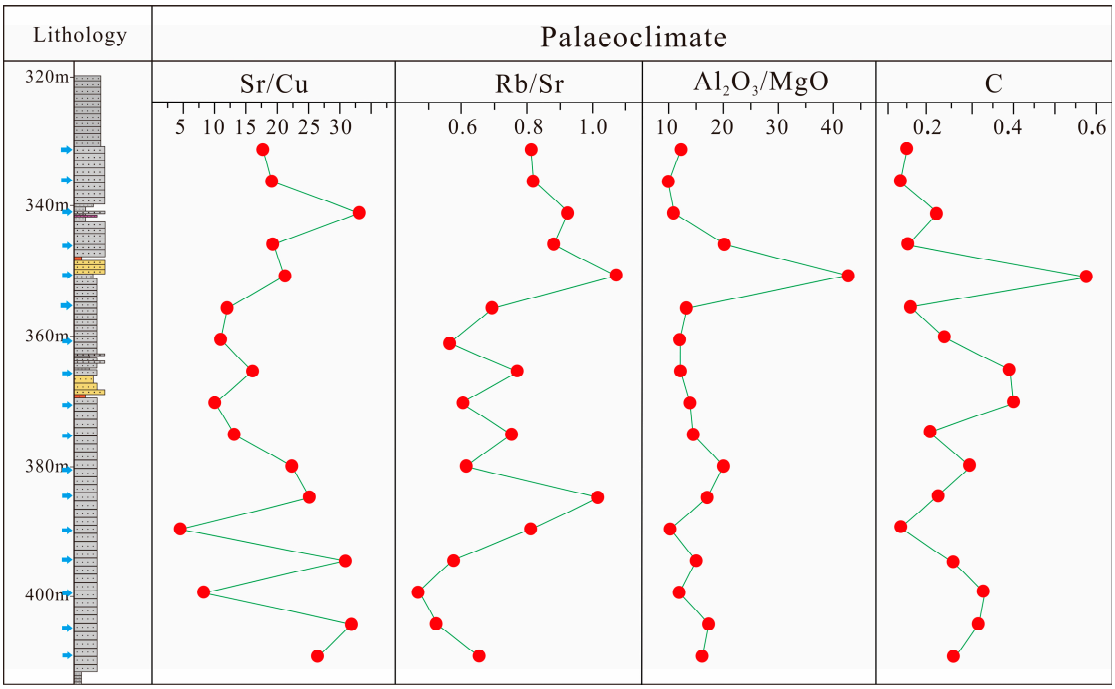

Figure 13. Paleoclimate change indicators in the Yimin Formation sandstone.

5.4.2. Paleoweathering in Provenance and Indications for Paleoclimate

The weathering, denudation, transport, sedimentary diagenesis, and post-generative alteration of clastic rocks can result in changes in the geochemistry of the rock. Therefore, major and trace elements can be used to assess the sedimentary climate, compositional maturity, weathering degree, and alteration of sandstones [64,65].

The CIA (chemical index of alteration) can be used to determine the degree of weathering in the source area. CIA values between 50 and 65, 65 and 80, and 80 and 100, respectively, reflect a low degree of weathering under arid climate conditions, a moderate degree of weathering under warm and wet conditions, and an intense degree of weathering under hot and wet conditions [66]. The CIA values of the Yimin Formation sandstone range from 51.86 to 67.32, indicating that the source area of the Yimin Formation has suffered a low degree of alteration. In the SiO_2-(Al_2O_3 + K_2O + Na_2O) paleoclimate discrimination diagram (Figure 14a), all samples fall into the arid-to-semi-arid region. Values of ICV < 1 indicate mature samples rich in clay minerals, which may indicate cyclic sedimentation or the first sediments under intense weathering, and CV > 1 indicates immature samples that are the first sediments in the background [29]. The ICV values of the sandstone samples range from 0.96 to 1.39, with an average of 1.08, indicating that the Yimin Formation sandstones are the first sediments in the background of tectonic activity. The samples were controlled by source rocks and did not experience intense chemical weathering. Nesbitt and Young (1984) established the A-CN-K triangulation, which can represent the CIA value. The three end elements are Al_2O_3, CaO* + Na_2O, and K_2O. In the CIA-ICV diagram (Figure 14b), all samples fall in the region of weak weathering, indicating that the Yimin Formation is

characterized by immaturity, and that the source of the material originated from the upper crust. In the A-CN-K diagram (Figure 14c), most samples follow the weathering tendency of granite, suggesting that the source rock was mainly granite. The CIA value of the Yimin Formation is concentrated in the range from 60 to 70, indicating that the weathering of granite in the source area of the Yimin Formation is weak.

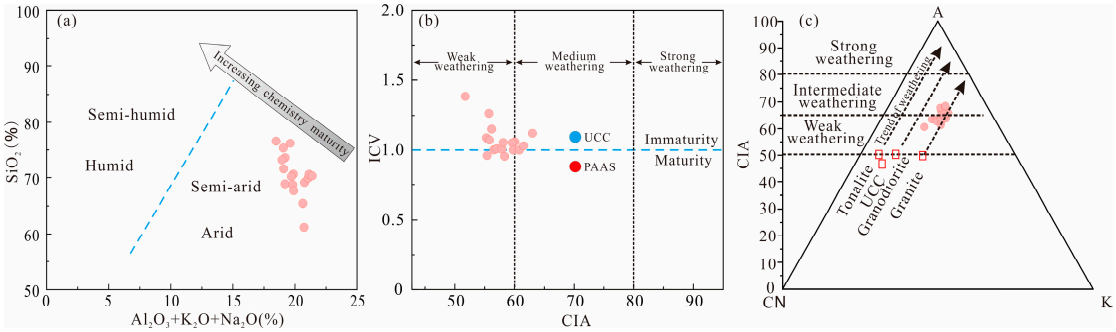

Figure 14. Diagram of paleoenvironmental discrimination of the Yimin Formation sandstone. (**a**) SiO_2-(Al_2O_3 + K_2O + Na_2O) diagram [67]. (**b**) ICV-CIA diagram [29]. (**c**) A-CN-K diagram [68]. UCC: upper continental crust. PAAS: post-archean Australian shale.

5.5. The Enrichment Mechanism of Uranium

The shape of coffinite and its co-existence with pyrite are clearly visible under BSE. Coffinite in an irregular granular or colloidal form within framboidal pyrite (Figure 5a) or between submicron cubic pyrite crystals (Figure 5b), and coffinite tightly cemented with framboidal pyrite (Figure 5c) were observed in the samples. The Fe^{2+} in pyrite is believed to play a critical role in the reduction and precipitation of hexavalent uranium. The negative valent sulfur (S^{2-}) in pyrite acts as a reducing agent, and together with Fe^{2+}, creates a microzone-reducing environment, thereby directly reducing hexavalent uranium [69,70].

Coffinite is distributed in stellate and micro-vein forms at the edges, cracks, or dissolution pits of detrital quartz, potassium feldspar, and biotite (Figure 5d–f). Alkaline feldspar produces a large amount of K_2O during the alteration process of mineralized sandstone, reacting with CO_2 in sandstone pore water to form K_2CO_3, and K_2CO_3 enters the pore aqueous solution to form alkaline solution, thus forming a local alkaline environment. Under alkaline conditions, quartz debris will dissolve, and this process provides a large amount of SiO_2. When U(VI) is reduced to U(IV) in $[UO_2]^{2+}$, a large amount of SiO_2 in the surrounding fluid participates in the reaction and combines with the U(IV) to form coffinite [71].

Some colloidal (Figure 5g), burr-like, or micro-columnar shapes around pyrite (Figure 5h) and anatase (Figure 5i) commonly occur in the cleavage cracks of biotite in uranium ores. During hydrolysis and chloritization, biotite exhibits expansion and loosening, while becoming more adsorbent. A large amount of Fe^{2+} precipitates in this process, creating a micro-reducing environment for uranium reduction and precipitation. U(VI) and SiO_2 in the fluid are adsorbed, reduced, and subsequently precipitated near the cleavage cracks of altered biotite in an alkaline reducing environment [72]. Parts of Fe^{2+} react with S^{2-} or H_2S, producing colloidal pyrite that fills up the cleavage cavities.

Based on the above research, uranium mineralization can be summarized as follows. Clay minerals and organic detritus in uranium-bearing sandstones adsorbed and fixed abundant uranium before enrichment or in the early ore-forming period. In the process of epigenetic alteration, the uraniferous fluid experienced a complex process of adsorption-reduction-deposition with the change in physical and chemical conditions. First, uranyl complex ions in the fluid discharge uranium near the geochemical barrier, which is then adsorbed by pyrite, organic matter, biotite, and other clay minerals, and in the alkaline reducing environment, U(VI) combines with Si^{4+} and Ti^{4+} to form coffinite and uranium-titanium oxide.

5.6. Uranium Mineralization Models

Based on the geological characteristics and the tectonic evolution of the basin, this paper discusses the sandstone uranium mineralization process of the Kelulun Depression.

Initial tensile fracture and fault depression stage in the Late Jurassic: The Hailar Basin was in a long-term compressive state under the influence of the subduction of the Kula Plate below the Eurasian Plate [6]. The northwest-southeast thrust nappe structure indicates that the study area represents a large-scale extensional tectonic environment with rifting volcanism, and intermediate and acidic volcanic rocks are widely developed [73].

Stretching and rapid subsidence of the Early Cretaceous fault depression: After the volcanic eruption period beginning in the Late Jurassic, the upper crust in the study area was transformed from a compressional system to an extensional setting, and the tectonic activity was very intense. The main sedimentary deposits were alluvial fans, fan deltas, semi-deep lakes, and deep lake deposits, and the sedimentary lithology and lithofacies changed greatly and only some small-scale sand bodies were formed. However, the buried depth was large and unstable, and no large-scale uplift or denudation were observed [74]. Therefore, it was difficult to form a certain scale of epigenous oxidation, which is not conducive to the development of uranium mineralization.

Early Cretaceous depression shrinkage stages: The tectonic environment was generally stable. The Yimin Formation was formed mainly as a set of coal-bearing clastic rocks, with loose sandstone as a whole, large-scale good lateral connectivity, and stable top and bottom mudstone water-barrier layers. These characteristics were beneficial for the transport of uranium containing oxygenated water and the formation of uranium ore bodies. In addition, owing to the abundant supply of uranium in the mother rock, the erosion source area, a certain degree of uranium pre-enrichment occurred when the sand body of the Yimin Formation was deposited.

Tectonic depression inversion stage from the end of the Early Cretaceous to the Late Cretaceous: Since the Early Cretaceous, there have been two periods of severe tectonic inversion and obvious uplifting, tilting, and denudation events throughout the area [75]. The first stage occurred from the end of the Early Cretaceous to the beginning of the Late Cretaceous, that is, from the deposition of the Yimin Formation to the deposition of the Qingyuangang Formation. A regional angular unconformity was formed between them, which was a sedimentary response to tectonic reversal caused by compression. At the same time, this stage also represented the cut-off point when the tectonic environment caused extensional-to-sandstone-type uranium deposits to form. However, the uplift and tilt effects were weak, which restricted the scale of the Yimin deposits to a certain extent. The second stage occurred after the end of the Late Cretaceous, when the Upper Cretaceous strata in the area were compressed and deformed, resulting in large-scale uplift and denudation of the Yimin Formation in the target layer, which resulted in increased hydraulic gradient, thus strengthening the "supplement-diameter-drainage" system of epigenetic fluids [76]. The paleoclimate changed from warm and humid to arid and semi-arid [77]. The Yimin formation contains abundant organic carbon, which is sufficient to reduce uranium in the oxidizing fluid, and can be used as a good adsorbent to accelerate the reduction of uranium, which is conducive to the enrichment and mineralization of uranium. This was the main mineralization stage of the sandstone-type uranium deposit in the Yimin Formation.

Depression shrinking stage from Paleogene to Neogene: Since the Neogene, the study area has been a stable tectonic environment [78]. This led to long-term rich uranium fluid transformation in the Yimin Formation in the wide and gentle slope belt in the northwestern part of the depression, resulting in the further enrichment of sandstone uranium mineralization.

Notably, the Kelulun Depression was high in the south and low in the north from its formation to the deposition of the Yimin Formation. The paleocurrent direction was mainly from southwest to northeast, and the sedimentation and subsidence centers were located in the northern part of the depression. This tectonic pattern of high in the south and low in the north lasted until the end of the Neogene, that is, the paleocurrent during the formation

period of the target layer was approximately the same as that during the mineralization period, which was conducive to the infiltration of uranium-containing oxygenated water into the mineralization process. The slow uplift at the later stage of the depression caused the epigenetic oxidation rate to be greater than the uplift denudation rate, which also enabled the ore body to be preserved.

Based on the above characteristics, the uranium mineralization process in the Kelulun depression was as follows: A large number of Mesozoic granites observed in the surrounding areas of Adunchulu, Arihashate, and New Barhuyouqi; U content from 2.7 to 22.3 ppm; Th content from 15.2 to 25.9 ppm [79]. These granites are uranium-rich structures. The Th/U ratio was 3.79–9.29, indicating the loss of uranium in uranium-rich granite [74]. In addition, the uranium content in the Yimin Formation sand body was relatively high (from 2.81 to 6.40 ppm), indicating that, during the process of weathering and denudation of the source rock, uranium-containing clasts migrated to the depression along with the groundwater and accumulated there, which further resulted in the uranium pre-enrichment. The Yimin Formation is dominated by medium-to-fine-grained sandstone with low compositional maturity, poor cementation, and good porosity and connectivity, which provided a migration channel for the long-distance transport of oxygenated uranium-carrying fluid. Moreover, the Yimin Formation sandstone contains large amounts of organic carbon and massive pyrite, formed in an environment conducive to uranium reduction and precipitation. Meanwhile, the climate gradually changed from warm and humid to an arid and semi-arid oxidizing sedimentary environment, which led to the leaching and migration of uranium and the formation of a uranium-rich oxidizing fluid. In addition, surface vegetation did not develop in the arid climate. Therefore, the uranium in the oxygen-rich surface water could migrate steadily into the basin (Figure 15a). In the Late Cretaceous-Neogene period, the basin was uplifted four times, strengthening the "replenishment, diameter, and drainage" system of supergene fluids. In the later period of deposition, the overall uplift of the Hailar Basin entered the transformation stage. In the early Late Cretaceous, the Yimin Formation was exposed at the surface for a long time, suffered from leaching, weathering, and denudation, and deposition was interrupted. The uranium- and oxygen-containing fluid that formed in the western depression infiltrated the strata of the Yimin Formation. The free $[UO_2]^{2+}$ in the uranium-rich fluid reacted with the reducing medium in the Yimin Formation, and the U(VI) in the uranium-containing fluid was reduced to U(IV), forming the most important uranium-bearing rock series. Finally, uranium ore bodies were formed in the redox transition zone of the Yimin Formation (Figure 15b).

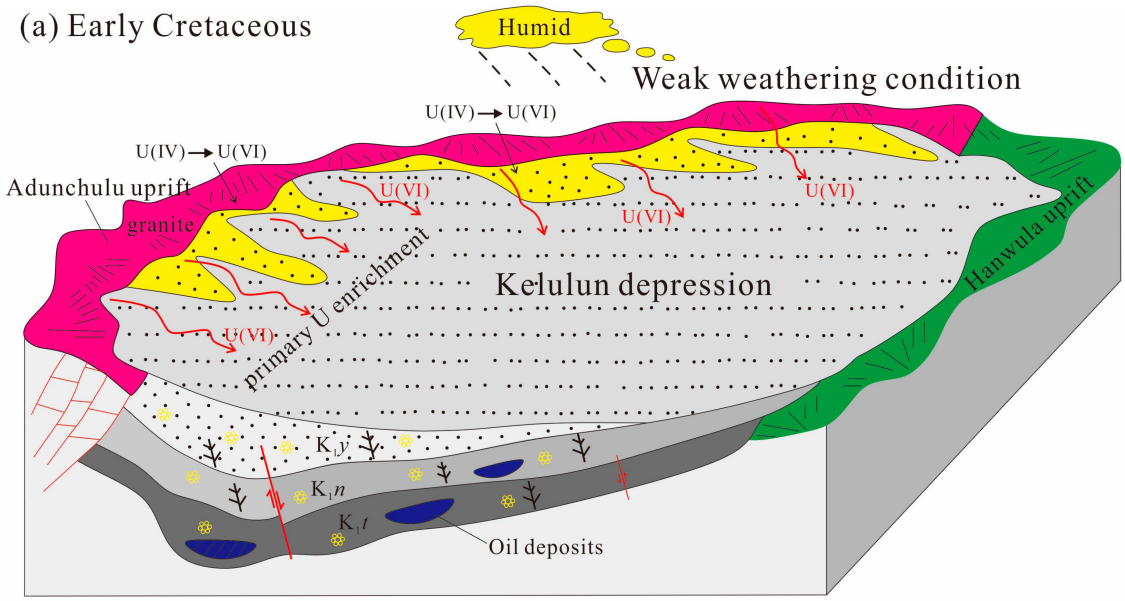

Figure 15. *Cont.*

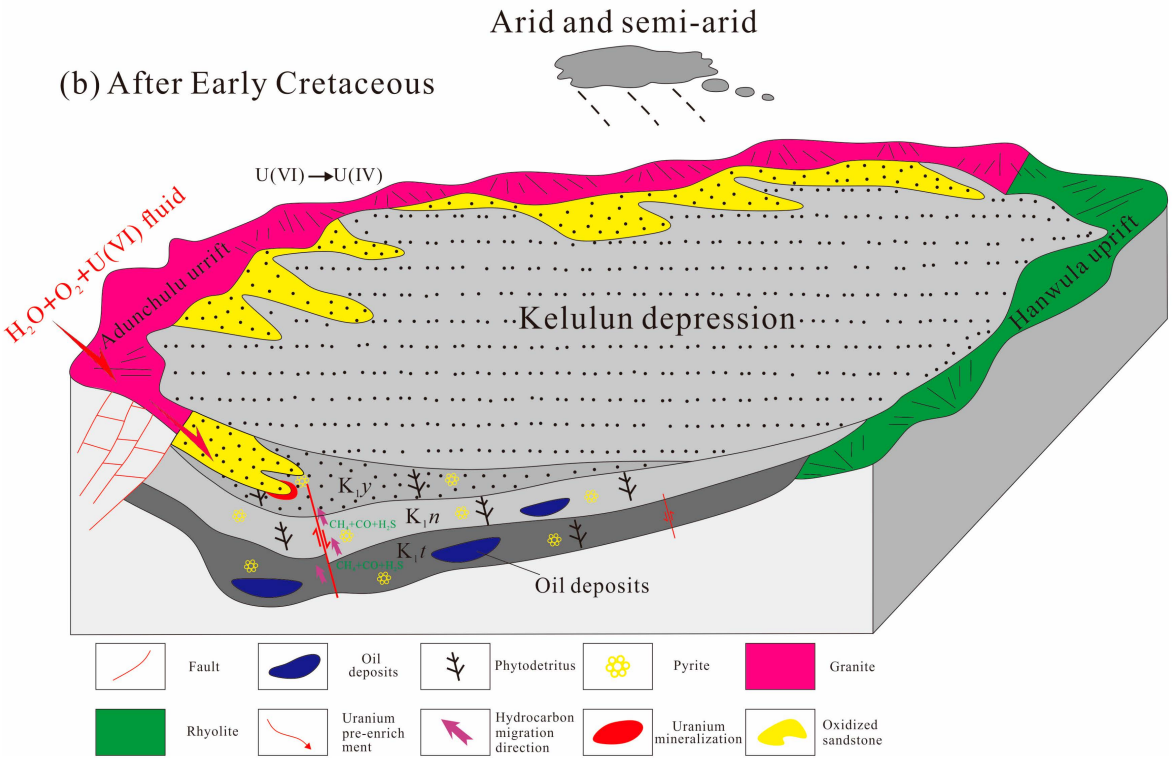

Figure 15. Metallogenic model for sandstone uranium deposits in the Kelulun Depression.

6. Conclusions

(1) Coffinite is present in the form of cement within and around pyrite or as stellate and irregular granular morphologies along the edges, fractures, or dissolution pits of detrital particles. Uranium-titanium oxide is produced in colloidal, burr-like, or micro-columnar shapes in the cleavage cracks of biotite;

(2) Geochemical analysis shows that the source rocks of the Yimin Formation are feldspar igneous rocks in the passive continental margin, and evolved under conditions of weak chemical weathering;

(3) The elemental Mo, U/Th, V/Cr, Ni/Co, and V/(V + Ni) ratios indicate that the paleo-water medium of the Yimin Formation was an oxygen-rich depositional environment, and the bottom water was moderately stratified and circulated smoothly. The C-value, Sr/Cu, Al_2O_3/MgO, and Rb/Sr ratios indicate that the Yimin Formation formed in an arid environment.

Author Contributions: Data curation, Z.Y. and X.Z.; Writing—original draft, F.M.; Writing—review & editing, F.N. and Q.W.; Supervision, D.S. and W.Z.; Project administration, F.X. All authors have read and agreed to the published version of the manuscript.

Funding: Mechanism of constraints of the basin and range coupling on uranium mineralization in the southern Great Xing'an Range and its lateral basins (Grant Number: U2244205); Metallogenic theory on sandstone-type uranium deposits and innovation of key technology as well as application of industry-university-research on uranium exploration (Funding Number: 20223AEI91003) and Study on Mechanism of Uranium Ultra Enrichment and Exploration Potential for Sandstone-type Uranium Deposit Hosted in the Cretaceous, Ordos Basin (Funding Number: NRE2021-02).

Data Availability Statement: All data generated or analyzed during this study are included in this article.

Acknowledgments: Special thanks go to the anonymous reviewers for their helpful suggestions and comments.

Conflicts of Interest: The authors declare that they have no known competing financial interests or personal relationships that could have appeared to influence the work reported in this paper.

References

1. Huang, S.H.; Qin, M.K.; Zhou, W.B.; Liu, Z.Y.; Liu, T.; Zhao, Z.W.; Dong, Y. Mineralization Conditions, Characteristics and Genesis of Sandstone-type Uranium Deposit of the Lower Member of Yimin Formation in Kelulun Sag of Inner Mongolia, China. *J. Earth Sci. Environ.* **2020**, *42*, 199–214. (In Chinese)
2. Ma, H.F.; Luo, Y.; Li, Z.Y.; Qin, M.K.; Wang, M.T. Characteristics of Sandbodies in Zalailuoer depression and analysis of uranium exploration direction. *Uranium Geol.* **2011**, *27*, 30–35. (In Chinese)
3. Zhang, H.Y.; Gao, B.; Ge, Q.; Hua, E.X.; Huang, S.H.; Yi, L.; Shen, W.; Lin, C.Y. The distribution and enrichment of Uranium in groundwater of Hailar Basin. *China Environ. Sci.* **2021**, *41*, 223–231. (In Chinese)
4. Zhong, Y.Q.; Xu, Q.X.; Gu, S.F. Application of Airborne Radioactivity Survey Data in Mineralization Prospect of Sandstone-type Uranium Deposit in Hailar Basin. *Geol. Resour.* **2010**, *19*, 319–324. (In Chinese)
5. Zhang, Z.J.; Yu, X.H.; Chen, Z.K.; Guo, Q.Y.; Luo, Y.; Zhang, C.H. Evolution of depositional system and uriniferous characteristics of Damoguaihe Formation in Kelulun Sag. *Uranium Geol.* **2005**, *21*, 23–29. (In Chinese)
6. Ma, H.F.; Luo, Y.; Wang, M.T.; Qi, D.N.; Li, J.H.; Fang, X.H. Analysis on mineralization conditions of ISL-amenable sandstone-type uranium deposits in Kelulun down-faulted basin, Inner Mongolia. *Uranium Geol.* **2006**, *22*, 83–89. (In Chinese)
7. Zhou, W.B.; Zhang, R.; Liu, T.; Mu, H.Q.; Zhao, Z.W.; Huang, X. Mineralization Geological Features and Prospective Study for Sandstone-type Uranium Deposit in Bel-Ulson Depression. *Northwest. Geol.* **2020**, *53*, 201–209. (In Chinese)
8. Jin, R.S.; Yu, R.A.; Yang, J.; Zhou, X.X.; Teng, X.M.; Wang, S.B.; Si, Q.H.; Zhu, Q.; Zhang, T.F. Pale-environmental Constraints on Uranium Mineralization in the Ordos Basin: Evidence from the Color Zoning of U-bearing Rock Series. *Ore Geol. Rev.* **2019**, *104*, 175–189. [CrossRef]
9. Nie, F.J.; Yan, Z.B.; Feng, Z.B.; Li, M.G.; Xia, F.; Zhang, C.Y.; Wang, Y.G.; Yang, J.X.; Kang, S.H.; Shen, K.F. Genetic models and exploration implication of the paleochannel sandstone-type uranium deposits in the Erlian Basin, North China-A review and comparative study. *Ore Geol. Rev.* **2020**, *127*, 103821. [CrossRef]
10. Rong, H.; Jiao, Y.Q.; Liu, W.H.; Cao, M.Q.; Yu, J.X.; Wu, L.Q.; Li, Q.C. Effects of Basic Intrusions on REE Mobility of Sandstones and Their Geological Significance: A Case Study from the Qianjiadian Standstone-hosted Uranium Deposit in the Songliao Basin. *Appl. Geochem.* **2021**, *120*, 104665. [CrossRef]
11. Lu, M.; Ye, R.; Zhang, B.M. Source identification of the geochemical anomaly from the fine-grained soil survey in the Nuheting sandstone-type uranium deposit, Erlian Basin, north China. *J. Geochem. Explor.* **2021**, *227*, 106797. [CrossRef]
12. Dimitrios, R.; Raymond, M.; Michel, C.; Olivier, P.; Marc, B. Conditions for uranium biomineralization during the formation of the Zoovch Ovoo roll-front-type uranium deposit in East Gobi Basin, Mongolia. *Ore Geol. Rev.* **2021**, *138*, 104351.
13. Ren, Y.S.; Yang, X.Y.; Miao, P.S.; Hu, X.W.; Chen, Y.; Chen, L.L.; Zhao, H.L. Mineralogical and geochemical research on Pengyang deposit: A peculiar eolian sandstone-hosted uranium deposit in the southwest of Ordos Basin. *Ore Geol. Rev.* **2022**, *141*, 104571. [CrossRef]
14. Cheng, X.Y.; Zhang, T.F.; Cheng, Y.H.; Liu, X.; Hu, P.; Wu, Z.Y. Element geochemical characteristics of the Middle-Late Jurassic microclastic rock in the Easthern Junggar Basin: Implications for tracing sediment sources and paleoenvironment restoration. *Geol. Bull. China* **2022**, *41*, 1950–1966. (In Chinese)
15. Dan, Z.B. Geochemical characteristics of the upper cretaceous Yaojia Formation in the southwest margin of Songliao Basin and its paleoenvironmental implication. *Nat. Resour. Inf.* **2022**, *49*, 22–32.
16. Maximilien, M.; Julie, A.; Jean, B.B.; Jean, R.; Madeleine, S.; Etienne, B.; Emmanuel, F.; Shrema, B.; Thierry, A. Unraveling weathering episodes in Tertiary regoliths by kaolinite dating (Western Ghats, India). *Gondwana Res.* **2019**, *69*, 89–105.
17. Hu, X.W.; Yang, X.Y.; Ren, Y.S.; Du, G.F.; Wu, Z.J. Genesis of interlayer oxidation zone-type uranium deposit in the channel conglomerates, Beisantai area, Junggar Basin: An insight into uranium mineralization. *Ore Geol. Rev.* **2022**, *140*, 104557. [CrossRef]
18. Yu, C.L.; Mu, N.N.; Huang, W.H.; Xu, W.H.; Feng, X.K. Major and Rare Earth Element Characteristics of Late Paleozoic Coal in the Southeastern Qinshui Basin: Implications for Depositional Environments and Provenance. *ACS Omega* **2022**, *7*, 30856–30878. [CrossRef] [PubMed]
19. Zhu, M.Y.; Shao, L.Y.; Sun, B.; Yao, H.P.; Spina, A.; Ma, S.M.; Wang, S.; Fan, J.Y.; Li, J.N.; Yan, S. Sequence Paleogeography and Coal Accumulation Model in the Fluvio-lacustrine Rift Basin: The Lower Cretaceous of the Huhehu Sag of Hailar Basin, Inner Mongolia (NE China). *Mar. Pet. Geol.* **2022**, *145*, 105879. [CrossRef]
20. Jia, R.K.; Liu, J.L.; Han, Q.C.; Zhao, S.M.; Shang, N.D.; Tang, P.Q.; Zhang, Y.Q. Mineral Matter Transition in Lignite During Ashing Process: A Case Study of Early Cretaceous Lignite from the Hailar Basin, Inner Mongolia, China. *Fuel* **2022**, *328*, 125252. [CrossRef]
21. Peng, W.; Song, Y.M.; Yang, X.; Zhou, Y.; Wang, Z.G. Reservoir-forming conditions in Bayanhushu Sag of Hailar Basin. *Acta Pet. Sin.* **2006**, *27*, 18–24. (In Chinese)
22. Zhang, L.T. The Tectonic Characteristics and Its Effect on the Control of the Oil and Gas Accumulation in Bayanhushu Sag. Master's Thesis, Northeast Petroleun University, Daqing, China, 2013. (In Chinese)

23. Jia, J.H.; Tao, S.Z.; Fang, X.; Hou, Y.P. Deep Jurassic volcano-sedimentary succession, reservoir-seal assemblage and their exploration significance in Northeast China: A case study of Jurassic in the Hailar basin. *Acta Geol. Sin.* **2021**, *95*, 377–395. (In Chinese)
24. Guo, B.; Shao, L.Y.; Hilton, J.; Wang, S.; Zhang, L. Sequence Stratigraphic Interpretation of Peatland Evolution in Thick Coal Seams: Examples from Yimin Formation (Early Cretaceous), Hailar Basin, China. *Int. J. Coal Geol.* **2018**, *196*, 211–231. [CrossRef]
25. Wang, S.; Shao, L.Y.; Li, J.X.; Li, J.N.; Timothy, J.; Zhu, M.Y.; Zhou, J.M. Coal Petrology of the Yimin Formation (Albian) in the Hailar Basin, NE China: Paleoenvironments and Wild-fires During Peat Formation. *Cretac. Res.* **2021**, *124*, 104815. [CrossRef]
26. Chen, F.; Hegner, E.; Todt, W. Zircon ages and Nd isotopic and chemical compositions of orthogneisses from the Black Forest, Germany: Evidence for a Cambrian magmatic arc. *Int. J. Earth Sci.* **2000**, *88*, 791–802. [CrossRef]
27. Li, J.; Huang, X.L. Mechanism of Ta-Nb enrichment and magmatic evolution in the Yashan granites, Jiangxi Provenance, South China. *Acta Petrol.* **2013**, *29*, 4311–4322. (In Chinese)
28. Roser, B.P.; Korsch, R.J. Provenance signatures of sandstone-mudstone suites determined using discriminant function analysis of major-element data. *Chem. Geol.* **1988**, *67*, 119–139. [CrossRef]
29. Cox, R.; Low, D.R.; Cullers, R.L. The influence of sediment recycling and basement composition on evolution of mudrock chemistry in the southwestern United States. *Geochim. Cosmochim. Acta* **1995**, *59*, 2919–2940. [CrossRef]
30. Cao, H.; Guo, W.; Shan, X.; Ma, L.; Sun, P. Paleolimnological environments and organic accumulation of the Nenjiang Formation in the southeastern Songliao basin. China. *Oil Shale* **2015**, *32*, 5–24. [CrossRef]
31. Zhao, D.J.; Wang, X.Q. Geochemical characteristics of the Middle Triassic fine-grained clastic sedimentary rocks in Youjiang Basin and its implications for provenance and tectonic setting. *Geotecton. Metallog.* **2019**, *44*, 311–324. (In Chinese)
32. Rudnick, R.L.; Gao, S. Composition of the Continental Crust. In *The Crust: Treatise on Geochemistry*; Holland, H.D., Turekian, K.K., Eds.; The Pergamon Press: Oxford, UK, 2003; pp. 1–64.
33. Sun, S.S.; McDonough, W.F. Chemical and isotopic systematics of oceanic basalts: Implications for mantle composition and processes. *Geol. Soc. Lond Spec. Publ.* **1989**, *42*, 313–345. [CrossRef]
34. Niku, M.M.; Bikash, G.; Panchanan, D. Sandstone Geochemistry of Dalbuing Formation of Yinkiong Group, Arunachal Pradesh, NE India: Implications for Provenance, Paleoweathering and Tectonic Settings. *J. Geol. Soc. India* **2021**, *31*, 297–307.
35. Sebastian, Z.; Robert, H. Provenance of Cretaceous sandstones in the Banda Arc and their tectonic significance. *Gondwana Res.* **2019**, *67*, 1–20.
36. Luo, X.N.; Li, X.Y.; Cai, Y.Q.; Yi, C.; Zhang, Z.L.; Zhang, Y.Y.; Zhang, Y. Provenance and Tectonic Setting of Lower Cretaceous Huanhe Formation Sandstones, Northwest Ordos Basin, North-Central China. *Minerals* **2021**, *11*, 1376. [CrossRef]
37. Schieber, J.A. Combined petrographical geochemical provenance study of the Newland Formation, Mid-Proterozoic of Montana. *Geol. Mag.* **1992**, *129*, 223–237. [CrossRef]
38. Floyd, P.; Leveridge, B.E. Tectonic environment of the Devonian Gramscatho basin, south Cornwall: Framework mode and geochemical evidence from turbiditic sandstones. *J. Geol. Soc.* **1987**, *144*, 531–540. [CrossRef]
39. Floyd, P.A.; Winchester, J.A.; Park, R.G. Geochemistry and tectonic setting of Lewisian clastic metasediments from the Early Proterozoic Loch Maree Group of Gairloch, NW Scotland. *Precambrian Res.* **1989**, *45*, 203–214. [CrossRef]
40. Gu, X.X.; Liu, J.M.; Zheng, M.H. Provenance and tectonic setting of the Proterozoic turbidites in Hunan, south China: Geochemical evidence. *J. Sediment. Res.* **2002**, *72*, 393–407. [CrossRef]
41. Bhatia, M.R.; Crook, K.A.W. Trace element characteristics of graywackes and tectonic discrimination of sedimentary basins. *Contrib. Mineral. Petrol.* **1986**, *92*, 181–193. [CrossRef]
42. Shao, L.; Stattegger, K. Sandstone petrology and geochemistry of the Turpan Basin (NW China): Implications for the tectonic evolution of a continental basin. *J. Sediment. Res.* **2001**, *71*, 37–49. [CrossRef]
43. Mclennan, S.M.; Hemming, S.; Mcdaniel, D.K. Geochemical Approaches to Sedimentation, Provenance and Tectonics. *Geol. Soc. Am. Spec. Pap.* **1993**, *284*, 21–40.
44. Cullers, R.L.; Podkovyrov, V.N. Geochemistry of the Mesoproterozoic Lakhanda shalesin southeastern Yakutia, Russia: Implications for mineralogical and provenance control, and recycling. *Precambrian Res.* **2000**, *104*, 77–93. [CrossRef]
45. Taylor, S.R.; Mclennan, S.M. *The Continental Crust: Its Composition and Evolution Geoscience Texts*; Blackwell Scientific Publications: Hoboken, NJ, USA, 1985; pp. 1–312.
46. Bracciali, L.; Marroni, M.; Pandolfi, L. Geochemistry and petrography of Western Tethys Cretaceous sedimentary covers (Corsica and Northern Apennines): From source areas to configuration of margins. *Spec. Pap. Geol. Soc. Am.* **2007**, *420*, 73–93.
47. Sun, D.; Li, H.M.; Xia, F.; Nie, F.J.; Huang, G.W.; Zhang, Z.B.; Meng, F.M.; Pan, J.Y.; Hu, Y.J. Provenance and Tectonic Setting of the Lower Cretaceous Huanhe Formation in the Northwestern Ordos Basin and Its Implications for Uranium Mineralization. *ACS Omega* **2024**, *9*, 3324–3341. [CrossRef] [PubMed]
48. Christopher, B.; Kuiwu, L.; Oswald, G. Geochemistry of sandstones and shales from the Ecca Group, Karoo Supergroup, in the Eastern Cape Provenance of South Africa: Implications for provenance, weathering and tectonic setting. *Geoscience* **2017**, *9*, 340–360.
49. Maynard, J.B.; Valloni, R.; Yu, H.S. Composition of modern deep-sea sands from arc-related basins Leggett, J.K. Trench and Fore-arc sedimentation. *Geol. Soc. Lond. Spec. Publ.* **1982**, *10*, 551–561. [CrossRef]
50. Bhatia, M.R. Plate Tectonics and Geochemical composition of sandstones. *J. Geol.* **1983**, *91*, 611–627. [CrossRef]

51. Fang, G.Q. $K_2O/(Na_2O+CaO)$-SiO_2/Al_2O_3: One for pushing Discriminant map of plate tectonic background during fault flysch formation. *Geol. Northwest China Sci.* **1993**, *14*, 121–125. (In Chinese)
52. Jiang, Z.G. The main controlling factors and despotional model of organic matter accumulation in the Wufeng-Longmaxi formations in the Sichuan Basin. Master's Thesis, East China University of Techonlogy, Nanchang, China, 2018. (In Chinese)
53. Chen, L.Q.; Steel, R.J.; Guo, F.S.; Olariu, C.; Gong, C.L. Alluvial fan facies of the Yongchong Basin: Implications for tectonic and paleoclimatic changes during Late Cretaceous in SE China. *J. Asian Earth Sci.* **2017**, *134*, 37–54. [CrossRef]
54. Wei, W.; Algeo, T.J.; Lu, Y.; Liu, H.; Zhang, S.; Peng, L.; Zhang, J.; Chen, L. Identifying marine incursions into the Paleogene Bohai Bay Basin Lake system in northeastern China. *Int. J. Coal Geol.* **2018**, *200*, 1–17. [CrossRef]
55. Litf, T.H.; Xiao, X.M. Geochemical Characterization and Methane Adsorption Capacity of Overmature Organic-rich Lower Cambrian Shales in Northeast Guizhou Region, Southwest China. *Mar. Pet. Geol.* **2017**, *86*, 858–873.
56. Lin, L.; Algeo, T.J. Redox Changes in the Outer Yangtze Sea (South China) through the Hirnantian Glaciation and Their Implications for the End-Ordovician Biocrisis. *Earth Sci. Rev.* **2021**, *212*, 103443. (In Chinese)
57. Algeotj, L. Redox classification and calibration of redox thresholds in sedimentary systems. *Geochim. Cosmochim. Acta* **2020**, *287*, 8–26. [CrossRef]
58. Jones, B.; Manning, D.A.C. Comparison of geochemical indices used for the interpretation of palaeoredox conditions in ancient mudstones. *Chem. Geol.* **1994**, *111*, 111–129. [CrossRef]
59. Algeo, T.J.; Maynard, J.B. Trace element behavior and redox facies in core shales of upper Pennsy Ivanian Kansas type cyclotheme. *Chem. Geol.* **2004**, *206*, 289–318. [CrossRef]
60. Zhang, T.F.; Cheng, X.Y.; Wang, S.Y.; Miao, P.S.; Ao, C. Middle Jurassic-Early Cretaceous drastic paleoenvironmental changes in the Ordos Basin: Constraints on sandstone-type uranium mineralization. *Ore Geol. Rev.* **2022**, *142*, 104652. [CrossRef]
61. Zhang, Z.B.; Xu, Y.; Miao, Y.J.; Wang, W.F.; Zhao, D.F.; Chen, D.L. Provenance and Sedimentary Environment of Paleogene Gongjue Formation in Qamdo Basin. *Acta Sedimentol. Sin.* **2022**, *40*, 1561–1581. (In Chinese)
62. Zhang, X.G.; Lin, C.Y.; Muhammad, A.Z.; Jia, X.P.; Zhang, T. Paleosalinity and water body type of Eocene Pinghu Formation, Xihu Depression, East China Sea Basin. *J. Pet. Sci. Eng.* **2017**, *158*, 469–478. [CrossRef]
63. Li, Y.; Nie, F.J.; Jia, L.C.; Lu, S.J.; Yan, Z.B. Geochemical Characteristics, Palaeoenvironment and Provenance of Uranium-Bearing Sandstone in the Sifangtai Formation, Northern Songliao Basin, Northeast China. *Minerals* **2021**, *11*, 1019. [CrossRef]
64. Bokanda, E.E.; Ekomane, E.; Kenfack, N.G.R.; Njilah, K.L.; Ashukem, N.E.; Tematio, P.; Bisse, S.B.; Ngueutchoua, G.; Orock, N.S.; Belinga, C. Provenance, paleoclimate and diagenetic signatures of sandstones in the Mamfe Basin (West Africa). *Heliyon* **2019**, *2*, e01140.
65. Sageman, B.B.; Murphy, A.E.; Werne, J.P. Atale of shales: The relative roles of production, decomposition, and dilution in the accumulation of organic rich strata, Middle upper Devonian, Appalachiam Basin. *Chem. Geol.* **2003**, *195*, 229–273. [CrossRef]
66. Md, A.R.; Sudeb, C.D.; MarkI, P.; James, T.; Md, S.A.; Mohammad, N.Z. Geochemistry of Recent Brahmaputra River Sediments: Provenance, Tectonics, Source Area Weathering and Depositional Environment. *Minerals* **2020**, *10*, 813. [CrossRef]
67. Suttner, L.J.; Dutta, P.K. Alluvial sandstone composition and paleoclimate. Framework mineralogy. *J. Sediment. Petrol.* **1986**, *56*, 329–345.
68. Nesbitt, H.W.; Young, G.M. Prediction of some weathering trends of plutonic and volcanic rocks based on thermodynamic and kinetic considerations. *Geochim. Cosmochim. Acta* **1984**, *48*, 1523–1534. [CrossRef]
69. Liu, J.; Nie, F.J.; Hou, S.R.; Chen, L.L.; Wang, J.L. Types of uranium mineral and its occurrence state of the sandstone-type uranium deposits in the Meso-cenozoic basin. East China Inst. *Technol. Nat. Sci.* **2013**, *36*, 107–112. (In Chinese)
70. Chen, L.L.; Chen, Y.; Guo, H.; Zhao, H.L.; Miao, P.S.; Li, J.G.; Feng, X.X.; Yu, R.A.; Tang, C. Characteristics of Altered Ilmenite in Uranium-Bearing Sandstone and Its Relationship with Uranium Minerals in the Northeastern Ordos Basin. *J. Earth Sci.* **2021**, *33*, 342–357. [CrossRef]
71. Li, H.M.; Li, L.; Peng, Y.B.; Wang, G.; Luo, X.N.; Yi, C. Characteristics of clay minerals in sandstone-type uranium deposits in the northern Ordos Basin and their geological significances. *Acta Mineral. Sin.* **2020**, *40*, 539–548. (In Chinese)
72. Chen, L.L.; Chen, Y.; Feng, X.X.; Li, J.G.; Guo, H.; Miao, P.S.; Jin, R.S.; Tang, C.; Zhao, H.L.; Wang, G.; et al. Uranium occurrence state in the Tarangaole area of the Ordos Basin, China: Implications for enrichment and mineralization. *Ore Geol. Rev.* **2019**, *115*, 103034.
73. Huang, S.H.; Zhou, W.B.; Dong, Y.; Qin, M.K. Characteristics of host sand body and its uranium mineralization potential of the upper member of Yimin Formation in Bei'er Depression, Hailar Basin. *Northwest. Geol.* **2021**, *54*, 166–178. (In Chinese)
74. Wang, W.Q.; Liu, C.Y.; Wang, J.Q.; Ma, H.H.; Guan, Y.Z. Characteristics of uranium content and its geological and mineralization significance for the provenance areas, northern northwest China. *Earth Sci. Front.* **2019**, *26*, 292–303. (In Chinese)
75. Yang, X. Recovery of the prototype basin and structural evolution for Bayanhushu Sag. *Pet. Geol. Oilfield Dev. Daqing* **2020**, *39*, 18–25. (In Chinese)
76. Shang, Y.; Chen, J.L.; Lin, C.H.; Fan, L.G. Characteristics of late cretaceous tectonic inversion for China Northeast Basin group. *Pet. Geol. Oilfield Dev. Daqing* **2021**, *40*, 26–31. (In Chinese)
77. Ma, Y.L. Study on sedimentary and reservior characteristics of Bayanhushu Sag. Master's Thesis, Northeast Petroleum University, Daqing, China, 2014. (In Chinese).

78. Sun, X.M.; Lu, B.L.; Zhang, M.S.; Du, J.Y.; Xu, W.Q.; Tian, J.X. Typical structural styles and deformation sequence in Outcrop area of Hailar Basin and its margin. *J. Jilin Univ. (Earth Sci. Ed.)* **2011**, *S1*, 9. (In Chinese)
79. Xia, Y.L.; Liu, H.B. Research on supplying potential of uranium source from rocks. *Uranium Geol.* **2006**, *22*, 99–103. (In Chinese)